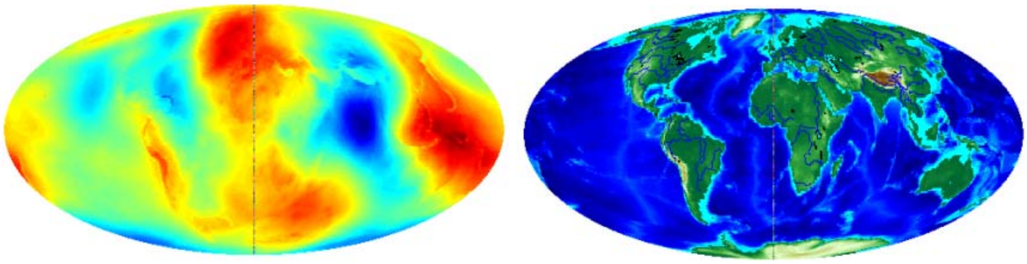

Siegen Preprints on Geomathematics

Electro-Magneto-Encephalography for the three-Shell Model: Numerical Implementation for Distributed Current in Spherical Geometry

A.S. Fokas[1], O. Hauk[2], and V. Michel[3]

[1]*Department of Applied Mathematics and Theoretical Physics, University of Cambridge, Cambridge, CB3 0WA, UK*

[2]*MRC Cognition and Brain Sciences Unit, Cambridge, CB2 7EF, UK*

[3]*Geomathematics Group, Department of Mathematics, University of Siegen, Germany*

www.geomathematics-siegen.de

6

Electro-Magneto-Encephalography for the three-Shell Model: Numerical Implementation for Distributed Current in Spherical Geometry

A.S.Fokas[1] & O.Hauk[2] & V.Michel[3]
[1] *Department of Applied Mathematics and Theoretical Physics*
University of Cambridge
Cambridge, CB3 0WA, UK
[2] *MRC Cognition and Brain Sciences Unit*
Cambridge, CB2 7EF, UK
[3] *Geomathematics Group, Department of Mathematics*
University of Siegen
57068 Siegen, Germany

May 24, 2011

Abstract

The basic inverse problems for the functional imaging techniques of Electroencephalography (EEG) and Magnetoencephalography (MEG) consist of estimating the neuronal current in the brain from the measurement of the electric potential on the scalp and of the magnetic field outside the head. Here we present a rigorous derivation of the relevant formulae for a three-shell spherical model in the case of independent as well as simultaneous MEG and EEG measurements. Furthermore, we introduce an explicit and stable technique for the numerical implementation of these formulae. Numerical examples are presented using the locations and the normal unit vectors of the real 102 magnetometers and 70 electrodes of the Elekta Neuromag (R) system.

1 Introduction

For the study of real time brain processes, among the most important imaging techniques are electroencephalography (EEG) and magnetoencephalography (MEG) — for early works see, for example, [1, 2]. Taking into consideration that the language of mind is electrical signaling, it follows that EEG and MEG allow, in some sense, the recording in real time of “brain conversations”. In order to produce images of brain activation using either EEG or MEG it is necessary to solve certain mathematical inverse problems. Indeed, the neuronal current (the so-called primary current) creates an electric potential which can be measured on the scalp, as well as a magnetic field which can be measured outside the head. The relevant inverse problems for EEG and MEG involve the calculation of the neuronal current from the knowledge of the electric potential and the magnetic field respectively. However, as it was already known to Helmholtz since 1853, the solutions of these problems are non-unique.

For MEG, a complete answer to the non-uniqueness question for a homogeneous *spherical* model was presented in [3] and [4] where it was shown that: (a) The only part of a continuously distributed current that can be reconstructed via MEG consists of certain moments of one of the two functions specifying the tangential component of the current (the other function specifying the tangential component, as well as the radial component of the current are "invisible" in the spherical model of MEG). (b) It is possible to reconstruct uniquely the current that minimizes the L^2-norm. Some of these results were extended, from a spherical to a star-shape geometry in [5]. The mathematical notion of complementarity of MEG and EEG for a *spherical* geometry was introduced in [6] where it was shown that the component of a continuously distributed neuronal current which generates the electric potential (and hence measured by EEG) lives in the orthogonal complement of the component of the current which generates the magnetic potential (which is measured by MEG).

A straightforward approach for the solution of the inverse problems associated with simultaneous EEG and MEG measurements was introduced in [7]. This approach yields a complete answer to the non-uniqueness question even in the case of an arbitrary geometry. Furthermore, in the particular cases of spherical and ellipsoidal geometries it yields effective formulae for the "visible" component of the current.

In this paper: (a) We present the *rigorous* solution of the inverse problems associated with the spherical three-shell model in the case of independent as well as simultaneous EEG and MEG measurements. In the case of independent MEG measurements, the formula is identical to the one in [3], [4], but the derivation is much simpler. (b) We introduce an effective numerical implementation of the associated formulae for MEG and EEG, both for independent as well as simultaneous EEG and MEG measurements.

The spherical three-shell model consists of a sphere Ω_c modeling the space occupied by the cerebrum, surrounded by three concentric shells $\Omega_\mathrm{f}, \Omega_\mathrm{b}, \Omega_\mathrm{d}$, modeling the spaces occupied by the cerebrospinal fluid, the skull and the skin. These compartments are distinguished by their different values of electric conductivity, which will be denoted respectively by σ_c, σ_f, σ_b, σ_d. The domains $\Omega_\mathrm{c}, \Omega_\mathrm{f}, \Omega_\mathrm{b}, \Omega_\mathrm{d}$ are defined as follows:

$$\Omega_\mathrm{c} : 0 \leq r < c_1, \Omega_\mathrm{f} : c_1 < r < f_1, \Omega_\mathrm{b} : f_1 < r < b_1,$$
$$\Omega_\mathrm{d} : b_1 < r < d_1.$$

Also, Ω_{e} will denote the space defined by $r > d_1$. Moreover, Ω represents the unit sphere.
In the following, vectors are denoted by bold-face letters such as $\mathbf{r}$, $\boldsymbol{\tau}$, $\mathbf{Q}$, and $\mathbf{J}$, whereas their Euclidean norms are denoted by their corresponding non-bold-face counterparts, for example, r and τ. Moreover, the associated unit vectors are denoted by $\hat{\mathbf{r}} := r^{-1}\mathbf{r}$, $\hat{\boldsymbol{\tau}} := \tau^{-1}\boldsymbol{\tau}$, etc.

2 A Simple Derivation of the Result of [4] and its EEG Analogue

2.1 MEG

Proposition 2.1 *Let $\mathbf{Q}(\boldsymbol{\tau})$ be the moment of a dipole at the point $\boldsymbol{\tau}$ with $\tau < d_1$. Then, the corresponding magnetic potential $U^{\mathrm{D}}(\mathbf{r}, \boldsymbol{\tau})$ at the exterior Ω_{e} satisfies*

$$4\pi r \frac{\partial U^{\mathrm{D}}}{\partial r}(\mathbf{r}, \boldsymbol{\tau}) = -(\mathbf{Q}(\boldsymbol{\tau}) \times \boldsymbol{\tau}) \cdot \nabla_{\boldsymbol{\tau}} \frac{1}{|\mathbf{r} - \boldsymbol{\tau}|}, \quad \mathbf{r} \in \Omega_{\mathrm{e}}, \quad \tau < d_1. \tag{1}$$

Proof. Recall that

$$-\frac{4\pi}{\mu} \mathbf{r} \cdot \mathbf{B}^{\mathrm{D}}(\mathbf{r}) = \mathbf{r} \cdot \left(\mathbf{Q} \times \nabla_{\mathbf{r}} \frac{1}{|\mathbf{r} - \boldsymbol{\tau}|} \right). \tag{2}$$

Since $\tau < d_1$, B^{D} is obviously in $\mathrm{C}^{(\infty)}(\Omega_{\mathrm{e}})$. Using the definition of U^{D} (note that the Maxwell equations imply the existence of U^{D}), i.e.

$$\mathbf{B}^{\mathrm{D}} = \mu \nabla_{\mathbf{r}} U^{\mathrm{D}},$$

as well as the identity

$$\nabla_{\mathbf{r}} \frac{1}{|\mathbf{r} - \boldsymbol{\tau}|} = -\nabla_{\boldsymbol{\tau}} \frac{1}{|\mathbf{r} - \boldsymbol{\tau}|},$$

equation (2) becomes

$$4\pi \mathbf{r} \cdot \nabla_{\mathbf{r}} U^{\mathrm{D}} = \mathbf{r} \cdot \mathbf{Q} \times \nabla_{\boldsymbol{\tau}} \frac{1}{|\mathbf{r} - \boldsymbol{\tau}|}. \tag{3}$$

But the RHS of this equation equals

$$\mathbf{r} \cdot \mathbf{Q} \times \frac{(\mathbf{r} - \boldsymbol{\tau})}{|\mathbf{r} - \boldsymbol{\tau}|^3} = \boldsymbol{\tau} \cdot \mathbf{Q} \times \frac{(\mathbf{r} - \boldsymbol{\tau})}{|\mathbf{r} - \boldsymbol{\tau}|^3} = \boldsymbol{\tau} \cdot \mathbf{Q} \times \nabla_{\boldsymbol{\tau}} \frac{1}{|\mathbf{r} - \boldsymbol{\tau}|},$$

which equals the RHS of equation (1). Also

$$\mathbf{r} \cdot \nabla_{\mathbf{r}} U^{\mathrm{D}} = r \frac{\partial U^{\mathrm{D}}}{\partial r}$$

and hence equation (3) becomes equation (1). ■

Note that, in the following, $\mathbf{J}^{\mathrm{P}}$ denotes the primary current which is derived from the integration of terms including the dipole moment $\mathbf{Q}$. In a sense, it is the continuous analogue of the discrete dipole moment. Correspondingly, whereas U^{D} represents the magnetic potential of a single dipole, we will write U for the continuous version, i.e.

$$U(\mathbf{r}) := \int_{\Omega_{\mathrm{c}}} U^{\mathrm{D}}(\mathbf{r}, \boldsymbol{\tau}) \, \mathrm{dV}(\boldsymbol{\tau}).$$

Proposition 2.2 *Let* $\mathbf{J}^{\mathrm{P}}(\boldsymbol{\tau})$ *be supported in* Ω_{c} *and assume that it has sufficient smoothness so that Gauss's theorem can be applied. Then*

$$4\pi U(\mathbf{r}) = -\int_{\Omega_{\mathrm{c}}} \left\{ \left[\nabla_{\tau} \cdot (\mathbf{J}^{\mathrm{P}}(\boldsymbol{\tau}) \times \boldsymbol{\tau}) \right] \sum_{n=0}^{\infty} \frac{\tau^n}{r^{n+1}(n+1)} P_n(\hat{\mathbf{r}} \cdot \hat{\boldsymbol{\tau}}) \right\} \mathrm{dV}(\boldsymbol{\tau}), \; \mathbf{r} \in \Omega_{\mathrm{e}}, \tag{4}$$

where P_n *represents the Legendre polynomial of degree* n.

Proof. Using the basic identity

$$\frac{1}{|\mathbf{r} - \boldsymbol{\tau}|} = \sum_{n=0}^{\infty} \frac{\tau^n}{r^{n+1}} P_n(\hat{\mathbf{r}} \cdot \hat{\boldsymbol{\tau}}), \quad r > \tau, \tag{5}$$

in equation (1), dividing the resulting equation by r, integrating the result with respect to r and using the fact that U^{D} vanishes as $r \to \infty$, equation (1) yields

$$4\pi U^{\mathrm{D}}(\mathbf{r}, \boldsymbol{\tau}) = (\mathbf{Q}(\boldsymbol{\tau}) \times \boldsymbol{\tau}) \cdot \nabla_{\boldsymbol{\tau}} \sum_{n=0}^{\infty} \frac{\tau^n}{r^{n+1}(n+1)} P_n(\hat{\mathbf{r}} \cdot \hat{\boldsymbol{\tau}}), \quad \mathbf{r} \in \Omega_{\mathrm{e}}. \tag{6}$$

The above derivation involves interchanging integration with respect to $\mathrm{d}r$ with $\nabla_{\boldsymbol{\tau}} \sum_{n=0}^{\infty}$. This can be justified as follows: We investigate the series

$$\begin{aligned} &\sum_{n=0}^{\infty} \left(\hat{\boldsymbol{\tau}} \frac{\partial}{\partial \tau} + \frac{1}{\tau} \nabla^*_{\hat{\boldsymbol{\tau}}} \right) \frac{\tau^n}{r^{n+2}} \, P_n \left(\hat{\mathbf{r}} \cdot \hat{\boldsymbol{\tau}} \right) \\ &\quad = \sum_{n=1}^{\infty} \left(n \, \frac{\tau^{n-1}}{r^{n+2}} \, P_n \left(\hat{\mathbf{r}} \cdot \hat{\boldsymbol{\tau}} \right) \hat{\boldsymbol{\tau}} + \frac{\tau^{n-1}}{r^{n+2}} \, P_n' \left(\hat{\mathbf{r}} \cdot \hat{\boldsymbol{\tau}} \right) \left(\hat{\mathbf{r}} - \left(\hat{\boldsymbol{\tau}} \cdot \hat{\mathbf{r}} \right) \hat{\boldsymbol{\tau}} \right) \right), \end{aligned}$$

where $\nabla_{\boldsymbol{\tau}} = \hat{\boldsymbol{\tau}} \frac{\partial}{\partial \tau} + \frac{1}{\tau} \nabla^*_{\hat{\boldsymbol{\tau}}}$ is the usual decomposition of the gradient operator in its radial and angular parts. The series is, for fixed $\boldsymbol{\tau} \in \Omega_{\mathrm{c}}$, uniformly convergent with respect to $\mathbf{r} \in \Omega_{\mathrm{e}}$, since it is dominated by

$$\sum_{n=1}^{\infty} \left(n \, \frac{\tau^{n-1}}{r^{n+2}} + \frac{\tau^{n-1}}{r^{n+2}} \, \frac{n(n+1)}{2} \cdot 2 \right)$$

(see [8], p. 39 for the estimates of P_n and P_n'). Thus,

$$\begin{aligned}
&\nabla_{\boldsymbol{\tau}} \sum_{n=0}^{\infty} \frac{\tau^n}{r^{n+2}}\, P_n\left(\hat{\mathbf{r}} \cdot \hat{\boldsymbol{\tau}}\right) \\
&\quad = \sum_{n=1}^{\infty} \left(n\, \frac{\tau^{n-1}}{r^{n+2}}\, P_n\left(\hat{\mathbf{r}} \cdot \hat{\boldsymbol{\tau}}\right) \hat{\boldsymbol{\tau}} + \frac{\tau^{n-1}}{r^{n+2}}\, P_n'\left(\hat{\mathbf{r}} \cdot \hat{\boldsymbol{\tau}}\right) \left(\hat{\mathbf{r}} - \left(\hat{\boldsymbol{\tau}} \cdot \hat{\mathbf{r}}\right) \hat{\boldsymbol{\tau}}\right) \right).
\end{aligned}$$

Furthermore, for similar reasons the series

$$\begin{aligned}
&\sum_{n=1}^{\infty} \int_{\varrho}^{\infty} \left| n\, \frac{\tau^{n-1}}{r^{n+2}}\, P_n\left(\hat{\mathbf{r}} \cdot \hat{\boldsymbol{\tau}}\right) \hat{\boldsymbol{\tau}} + \frac{\tau^{n-1}}{r^{n+2}}\, P_n'\left(\hat{\mathbf{r}} \cdot \hat{\boldsymbol{\tau}}\right) \left(\hat{\mathbf{r}} - \left(\hat{\boldsymbol{\tau}} \cdot \hat{\mathbf{r}}\right) \hat{\boldsymbol{\tau}}\right) \right| \mathrm{d}r \Bigg|_{\varrho = r} \\
&\qquad \le \sum_{n=1}^{\infty} \left(\frac{n}{n+1} \cdot \frac{\tau^{n-1}}{r^{n+1}} + \frac{\tau^{n-1}}{r^{n+1}} \cdot \frac{1}{n+1}\, n(n+1) \right)
\end{aligned}$$

is convergent for all $\mathbf{r} \in \Omega_{\mathrm{e}}$. Consequently, the interchanging of the integration with the gradient operator and the summation is allowed.
Integrating (6) with respect to $\boldsymbol{\tau}$ (which represents the passing from the discrete case of a single dipole to the continuous case) and using Gauss's theorem yields the following:

$$\begin{aligned}
4\pi U(\mathbf{r}) = &\int_{\partial\Omega_{\mathrm{c}}} \mathbf{n} \cdot \left(\mathbf{J}^{\mathrm{P}}(\boldsymbol{\tau}) \times \boldsymbol{\tau}\right) \sum_{n=0}^{\infty} \frac{\tau^n}{r^{n+1}(n+1)} P_n(\hat{\mathbf{r}} \cdot \hat{\boldsymbol{\tau}})\, \mathrm{dS}(\boldsymbol{\tau}) \\
&- \int_{\Omega_{\mathrm{c}}} \left\{ \left[\nabla_{\tau} \cdot \left(\mathbf{J}^{\mathrm{P}}(\boldsymbol{\tau}) \times \boldsymbol{\tau}\right)\right] \sum_{n=0}^{\infty} \frac{\tau^n}{(n+1) r^{n+1}} P_n(\hat{\mathbf{r}} \cdot \hat{\boldsymbol{\tau}}) \right\} \mathrm{dV}(\boldsymbol{\tau}).
\end{aligned}$$

But $\mathbf{J}^{\mathrm{P}}(\boldsymbol{\tau})$ vanishes on $\partial\Omega_{\mathrm{c}}$ and thus equation (4) follows. ■

Remark 2.1 *Equation (6) shows that the component of* $\mathbf{J}^{\mathrm{P}}(\boldsymbol{\tau})$ *in the* $\hat{\tau}$ *direction does not contribute to the magnetic field generated by a single dipole. Thus, measurements of* U *yield the two components* $(\mathbf{J}^{\mathrm{P}})^{\theta}$ *and* $(\mathbf{J}^{\mathrm{P}})^{\varphi}$*. On the other hand, equation (4) shows that for a continuously distributed current, the measurement of* U *yields information only about the single function* $\nabla_{\tau} \cdot (\mathbf{J}^{\mathrm{P}}(\boldsymbol{\tau}) \times \boldsymbol{\tau})$*. Hence, we "lose information", i.e. we go from two functions to a single function, as a result of Gauss's theorem!*

Proposition 2.3 *Let* $\hat{\boldsymbol{\tau}}, \hat{\boldsymbol{\theta}}, \hat{\boldsymbol{\varphi}}$ *denote the unit vectors in the spherical directions of the point* $\boldsymbol{\tau}$*, i.e.*

$$\begin{aligned}
\hat{\boldsymbol{\tau}} &= (\sin\theta\cos\varphi, \sin\theta\sin\varphi, \cos\theta), \\
\hat{\boldsymbol{\theta}} &= (\cos\theta\cos\varphi, \cos\theta\sin\varphi, -\sin\theta), \\
\hat{\boldsymbol{\varphi}} &= (-\sin\varphi, \cos\varphi, 0).
\end{aligned}$$

Let $(J^{\tau}, J^{\theta}, J^{\varphi})$ *be the spherical components of* $\mathbf{J}^{\mathrm{P}}$*, i.e.,*

$$\mathbf{J}^{\mathrm{P}} = J^{\tau}\hat{\boldsymbol{\tau}} + J^{\theta}\hat{\boldsymbol{\theta}} + J^{\varphi}\hat{\boldsymbol{\varphi}}. \tag{7}$$

Then

$$\mathbf{J}^{\mathrm{P}} \times \boldsymbol{\tau} = \tau \left(J^{\varphi} \hat{\boldsymbol{\theta}} - J^{\theta} \hat{\boldsymbol{\varphi}} \right).$$

If J^{θ} *and* J^{φ} *are represented in the form*

$$J^{\theta} = \frac{1}{\tau}\left(G_{\theta} - \frac{1}{\sin\theta} F_{\varphi} \right), \quad J^{\varphi} = \frac{1}{\tau}\left(\frac{1}{\sin\theta} G_{\varphi} + F_{\theta} \right), \tag{8}$$

where $F, G \in \mathrm{C}^{(2)}(\Omega_{\mathrm{c}})$ *and the subscripts* θ, φ *refer to derivatives, then*

$$\nabla_{\tau} \cdot (\mathbf{J}^{\mathrm{P}} \times \boldsymbol{\tau}) = \frac{1}{\tau} \Delta_{\theta,\varphi} F, \quad \Delta_{\theta,\varphi} \doteqdot \frac{1}{\sin\theta}\left[\partial_{\theta} \sin\theta \partial_{\theta} + \frac{1}{\sin\theta} \partial_{\varphi}^{2} \right]. \tag{9}$$

Proof.

$$\nabla_{\tau} \cdot (\mathbf{J}^{\mathrm{P}} \times \boldsymbol{\tau}) = \frac{1}{\tau^{2} \sin\theta} \left\{ \tau(\tau \sin\theta J^{\varphi})_{\theta} + \tau(-\tau J^{\theta})_{\varphi} \right\}$$

$$= \frac{1}{\sin\theta} \left\{ (\sin\theta J^{\varphi})_{\theta} - (J^{\theta})_{\varphi} \right\} = \frac{1}{\tau \sin\theta} \left[(\sin\theta F_{\theta})_{\theta} + \frac{1}{\sin\theta} F_{\varphi\varphi} \right].$$

■

Theorem 2.1 *Let* $\mathbf{J}^{\mathrm{P}}$ *be expanded in the form (7), (8). Then*

$$4\pi U(\mathbf{r}) = -\int_{\Omega_{\mathrm{c}}} \left\{ \left[\Delta_{\theta,\varphi} F(\tau, \theta, \varphi) \right] \sum_{n=0}^{\infty} \frac{\tau^{n-1}}{r^{n+1}(n+1)} P_{n}(\hat{\mathbf{r}} \cdot \hat{\boldsymbol{\tau}}) \right\} \mathrm{dV}(\boldsymbol{\tau}). \tag{10}$$

Furthermore, if $F(\tau, \cdot, \cdot)$ *is expressed in terms of spherical harmonics* Y_{n}^{m} *as*

$$F(\tau, \theta, \varphi) = \sum_{n=0}^{\infty} \sum_{m=-n}^{n} f_{n}^{m}(\tau) Y_{n}^{m}(\theta, \varphi), \tag{11}$$

where

$$\sum_{n=0}^{\infty} \sum_{m=-n}^{n} \left| f_{n}^{m}(\tau) \right| n^{3+\varepsilon} < +\infty \tag{12}$$

for some $\varepsilon > 0$ *and for all* $\tau \in [0, c_{1}]$, *then*

$$U(\mathbf{r}) = \sum_{n=0}^{\infty} \sum_{m=-n}^{n} \frac{Y_{n}^{m}(\Theta, \Phi)}{r^{n+1}} \frac{n}{2n+1} \int_{0}^{c_{1}} \tau^{n+1} f_{n}^{m}(\tau) \, \mathrm{d}\tau, \quad \mathbf{r} \in \Omega_{\mathrm{e}}, \tag{13}$$

where (r, Θ, Φ) *denote the spherical coordinates of* $\mathbf{r}$.

Proof. Note that the summability condition (12) implies that

$$\sum_{n=0}^{\infty} \sum_{m=-n}^{n} \left(f_{n}^{m}(\tau) \right)^{2} n^{6+2\varepsilon} < +\infty,$$

which corresponds to the following embedding in Sobolev spaces:

$$F(\tau,\cdot,\cdot) \in \mathcal{H}_{3+\varepsilon}(\Omega) \subset \mathrm{C}^{(2)}(\Omega) \,\text{for all}\; \tau \in [0,c_1],$$

where Ω represents the unit sphere in $\mathbb{R}^3$. For further details we refer to [8], pp. 81-89. Moreover, due to condition (12) it is allowed to interchange $\Delta_{\theta,\varphi}$ with the limit of the Fourier series, since

$$\begin{aligned}\left|\sum_{n=0}^{\infty}\sum_{m=-n}^{n} f_n^m(\tau)\Delta_{\theta,\varphi}Y_n^m(\theta,\varphi)\right| &= \left|\sum_{n=0}^{\infty}\sum_{m=-n}^{n} f_n^m(\tau)[-n(n+1)]Y_n^m(\theta,\varphi)\right| \\ &\leq \sum_{n=0}^{\infty}\sum_{m=-n}^{n} |f_n^m(\tau)|\, n(n+1)\sqrt{\frac{2n+1}{4\pi}}\end{aligned}$$

is uniformly convergent on Ω for every $\tau \in [0,c_1]$.
Furthermore, using $\mathrm{dV} = \tau^2 \sin\theta\, \mathrm{d}\tau\, \mathrm{d}\theta\, \mathrm{d}\varphi$ and

$$\int_0^{2\pi}\int_0^{\pi} Y_n^m(\hat{\boldsymbol{\tau}})P_{n'}(\hat{\boldsymbol{\tau}}\cdot\hat{\mathbf{r}})\sin\theta\,\mathrm{d}\theta\,\mathrm{d}\varphi = \frac{4\pi}{2n+1}\,Y_n^m(\hat{\mathbf{r}})\delta_{nn'} \tag{14}$$

equation (10) immediately becomes equation (13). ■

Remark 2.2 (Relation between (13) and the result of [4]) *In [4] the problem was first mapped to a harmonic problem. This appears to be an unnecessary complication. In any case, it is straightforward to obtain the analogous result: Equation (1) yields*

$$4\pi U^{\mathrm{D}}(\mathbf{r},\boldsymbol{\tau}) = (\mathbf{Q}(\boldsymbol{\tau})\times\boldsymbol{\tau})\cdot\nabla_{\boldsymbol{\tau}}\left(\frac{1}{\tau}\partial_\tau^{-1}\frac{1}{|\mathbf{r}-\boldsymbol{\tau}|}\right). \tag{15}$$

Indeed,

$$4\pi U^{\mathrm{D}}(\mathbf{r},\boldsymbol{\tau}) = (\mathbf{Q}(\boldsymbol{\tau})\times\boldsymbol{\tau})\cdot\nabla_{\boldsymbol{\tau}}\left(-\partial_r^{-1}\frac{1}{r|\mathbf{r}-\boldsymbol{\tau}|}\right)$$

and it can be verified (using for example equation (5)) that

$$-\partial_r^{-1}\frac{1}{r|\mathbf{r}-\boldsymbol{\tau}|} = \frac{1}{\tau}\partial_\tau^{-1}\frac{1}{|\mathbf{r}-\boldsymbol{\tau}|}.$$

Integrating the RHS of equation (15) w.r.t. $\boldsymbol{\tau}$ *and using Gauss's theorem we find*

$$-\int_0^{2\pi}\int_0^{\pi}\int_0^{c_1}\frac{1}{\tau}(\Delta_{\theta,\varphi}F)\frac{1}{\tau}\partial_\tau^{-1}\frac{1}{|\mathbf{r}-\boldsymbol{\tau}|}\,\tau^2\sin\theta\,\mathrm{d}\tau\,\mathrm{d}\theta\,\mathrm{d}\varphi.$$

Then integrating by parts w.r.t. τ*, we obtain*

$$\begin{aligned}&-\int_0^{2\pi}\int_0^{\pi}\left[\partial_\tau^{-1}\left(\Delta_{\theta,\varphi}F(\tau,\theta,\varphi)\right)\right]\left(\partial_\tau^{-1}\frac{1}{|\mathbf{r}-\boldsymbol{\tau}|}\right)\Bigg|_{\tau=0}^{\tau=c_1}\sin\theta\,\mathrm{d}\theta\,\mathrm{d}\varphi \\ &+\int_0^{2\pi}\int_0^{\pi}\int_0^{c_1}\left[\partial_\tau^{-1}(\Delta_{\theta,\varphi}F(\tau,\theta,\varphi))\right]\frac{1}{|\mathbf{r}-\boldsymbol{\tau}|}\,\sin\theta\,\mathrm{d}\tau\,\mathrm{d}\theta\,\mathrm{d}\varphi.\end{aligned}$$

We have

$$\left(\partial_\tau^{-1} \frac{1}{|\mathbf{r}-\boldsymbol{\tau}|}\right)\Bigg|_{\tau=0} = \left(\sum_{n=0}^{\infty} \frac{1}{n+1}\, \frac{\tau^{n+1}}{r^{n+1}}\, P_n\left(\hat{\mathbf{r}}\cdot\hat{\boldsymbol{\tau}}\right)\right)\Bigg|_{\tau=0} = 0.$$

Using

$$\partial_\tau^{-1}(\Delta_{\theta,\varphi}F(\tau',\theta,\varphi)) = -\int_\tau^{c_1} \Delta_{\theta,\varphi}F(\tau',\theta,\varphi)\,\mathrm{d}\tau',$$

we get

$$4\pi U(\mathbf{r}) = -\int_{\Omega_{\mathrm{c}}} \frac{1}{|\mathbf{r}-\boldsymbol{\tau}|}\left(\frac{1}{\tau^2}\int_\tau^{c_1} (\Delta_{\theta,\varphi}F)(\tau',\theta,\varphi)\,\mathrm{d}\tau'\right)\mathrm{dV}(\boldsymbol{\tau}). \qquad (16)$$

Remark 2.3 (Relation with the minimization of [4]) *Let*

$$U(\mathbf{r}) = \sum_{n=0}^{\infty}\sum_{m=-n}^{n} \frac{c_n^m}{r^{n+1}} Y_n^m(\hat{\mathbf{r}}).$$

In [4], starting with equation (16) it was shown that the constants c_n^m *are given by*

$$c_n^m = \frac{n}{2n+1}\int_0^{c_1} \tau^{n+1} f_n^m(\tau)\,\mathrm{d}\tau. \qquad (17)$$

The derivation of (17) was based on the following: If h *is defined by*

$$h(\tau,\theta,\varphi) = \frac{1}{\tau^2}\int_\tau^{c_1} \Delta_{\theta,\varphi}F(\tau',\theta,\varphi)\,\mathrm{d}\tau' = \sum_{n=0}^{\infty}\sum_{m=-n}^{n} h_n^m(\tau) Y_n^m(\theta,\varphi),$$

then

$$h_n^m(\tau) = -\frac{n(n+1)}{\tau^2}\int_\tau^{c_1} f_n^m(\tau')\,\mathrm{d}\tau'. \qquad (18)$$

Furthermore,

$$c_n^m = -\frac{1}{1+2n}\int_0^{c_1} \tau^{n+2} h_n^m(\tau)\,\mathrm{d}\tau. \qquad (19)$$

Substituting (18) into (19) and using integration by parts we find equation (17). The advantage of the new derivation is that it yields directly (17) (see equation (13)).

2.2 EEG

Proposition 2.4 *Let* $\mathbf{Q}(\boldsymbol{\tau})$ *be the moment of a dipole at the point* $\boldsymbol{\tau}$*. Then, the corresponding electric potential at the scalp is given by*

$$u_{\mathrm{s}}^{\mathrm{D}}(\mathbf{r},\boldsymbol{\tau}) = \frac{1}{4\pi}\mathbf{Q}(\boldsymbol{\tau})\cdot\nabla_{\boldsymbol{\tau}}\sum_{n=0}^{\infty} s_n \tau^n P_n(\hat{\boldsymbol{\tau}}\cdot\hat{\mathbf{r}}), \quad r = d_1,\ \tau < d_1, \qquad (20)$$

where the constant s_n *depends on the conductivities and the geometric characteristics.*

Proof. See [18]. ■

In analogy to the MEG case, we will write u_{s} for the continuous analogue of $u_{\mathrm{s}}^{\mathrm{D}}$.

Theorem 2.2 *Let*

$$\mathbf{J}^{\mathrm{P}}(\boldsymbol{\tau}) = \nabla_{\boldsymbol{\tau}}\Psi(\boldsymbol{\tau}) + \nabla_{\boldsymbol{\tau}} \times \mathbf{A}(\boldsymbol{\tau}), \quad \nabla_{\boldsymbol{\tau}} \cdot \mathbf{A}(\boldsymbol{\tau}) = 0, \tag{21}$$

with $\Psi \in \mathrm{C}^{(2)}(\Omega_{\mathrm{c}}, \mathbb{R}) \cap \mathrm{C}^{(1)}(\overline{\Omega_{\mathrm{c}}}, \mathbb{R})$ *and* $\mathbf{A} \in \mathrm{C}^{(2)}(\Omega_{\mathrm{c}}, \mathbb{R}^3) \cap \mathrm{C}^{(1)}(\overline{\Omega_{\mathrm{c}}}, \mathbb{R}^3)$*. Then the electric potential at the scalp is given by*

$$u_{\mathrm{s}}(\mathbf{r}) = -\frac{1}{4\pi}\int_{\Omega_{\mathrm{c}}} (\Delta\Psi(\boldsymbol{\tau})) \sum_{n=0}^{\infty} s_n \tau^n P_n(\hat{\boldsymbol{\tau}} \cdot \hat{\mathbf{r}})\, \mathrm{dV}(\boldsymbol{\tau}), \quad r = d_1. \tag{22}$$

Furthermore, if Ψ *is expanded in the form*

$$\Psi(\boldsymbol{\tau}) = \sum_{n=1}^{\infty}\sum_{m=-n}^{n} \psi_n^m(\tau) Y_n^m(\hat{\boldsymbol{\tau}}), \tag{23}$$

where $\{\psi_n^m(\tau)\}_{n=1,2,\ldots;\, m=-n,\ldots,n}$ *satisfies the summability condition (12), then*

$$u_{\mathrm{s}}(\mathbf{r}) = -\sum_{n=1}^{\infty}\sum_{m=-n}^{n} \frac{s_n}{2n+1} c_1^{n+1} \left[c_1 \dot{\psi}_n^m(c_1) - n\psi_n^m(c_1)\right] Y_n^m(\hat{\mathbf{r}}), r = d_1. \tag{24}$$

Proof. Integrating (20) with respect to $\mathrm{dV}(\boldsymbol{\tau})$ over Ω_{c}, using Gauss's theorem for the RHS, and noting that

$$\nabla \cdot \mathbf{J}^{\mathrm{P}} = \nabla \cdot (\nabla\Psi + \nabla \times \mathbf{A}) = \Delta\Psi,$$

equation (20) becomes equation (22).
Replacing in (22) Ψ by the RHS of (23) and using the identity

$$\tau^2 \Delta\psi_m^n(\tau) Y_n^m(\hat{\boldsymbol{\tau}}) = \left[\frac{\mathrm{d}}{\mathrm{d}\tau}\left(\tau^2 \frac{\mathrm{d}}{\mathrm{d}\tau}\psi_n^m(\tau)\right) - n(n+1)\psi_n^m(\tau)\right] Y_n^m(\hat{\boldsymbol{\tau}}),$$

as well as the orthogonality relation (14), equation (22) yields

$$u_{\mathrm{s}}(\mathbf{r}) = \tag{25}$$
$$-\sum_{n=1}^{\infty}\sum_{m=-n}^{n} \frac{s_n}{2n+1}\left\{\int_0^{c_1}\left[\frac{\mathrm{d}}{\mathrm{d}\tau}\left(\tau^2 \frac{\mathrm{d}}{\mathrm{d}\tau}\psi_n^m(\tau)\right) - n(n+1)\psi_n^n(\tau)\right]\tau^n\, \mathrm{d}\tau\right\} Y_n^m(\hat{\mathbf{r}}).$$

Note that the application of Δ to (23) was considered here in analogy to the proof of Theorem 2.1. Integration by parts yields

$$\int_0^{c_1}\left[\frac{\mathrm{d}}{\mathrm{d}\tau}\left(\tau^2 \frac{\mathrm{d}}{\mathrm{d}\tau}\psi_n^m(\tau)\right)\right]\tau^n\, \mathrm{d}\tau =$$
$$c_1^{n+1}\left[c_1\dot{\psi}_n^m(c_1) - n\psi_n^m(c_1)\right] + n(n+1)\int_0^{c_1}\psi_n^m(\tau)\tau^n\, \mathrm{d}\tau,$$

hence equation (25) becomes equation (24). ■

Remark 2.4 (Relation with the harmonic kernel) *In the case of the homogeneous sphere, it is straightforward (but again unnecessary) to rewrite equation (22) in terms of the harmonic kernel. Indeed, for the homogeneous case the constant* s_n *is given by*

$$s_n = \frac{1}{\sigma d_1^{n+1}} \frac{2n+1}{n+1} = \frac{1}{\sigma d_1^{n+1}} \left[2 - \frac{1}{n+1} \right].$$

Thus, the term $s_n \tau^n$ *gives the two terms*

$$\frac{2}{\sigma} \frac{\tau^n}{d_1^{n+1}}, \qquad -\frac{1}{\sigma} \frac{\tau^n}{d_1^{n+1}(n+1)} \tag{26}$$

and since

$$\sum_{n=0}^{\infty} \frac{\tau^n}{d_1^{n+1}} P_n(\hat{\mathbf{r}} \cdot \hat{\boldsymbol{\tau}}) = \frac{1}{|\mathbf{r} - \boldsymbol{\tau}|}\Big|_{r=d_1},$$

the first of the terms (26) yields immediately the harmonic kernel. Regarding the second term we note that

$$\begin{aligned} \int_0^{c_1} \tau^n (\Delta\Psi(\boldsymbol{\tau})) \tau^2 \frac{\mathrm{d}\tau}{n+1} &= \int_0^{c_1} \frac{\tau^{n+1}}{n+1} (\tau \Delta\Psi(\boldsymbol{\tau}))\, \mathrm{d}\tau \\ &= \int_0^{c_1} \tau^n \left\{ \int_\tau^{c_1} \tau' (\Delta\Psi(\boldsymbol{\tau}'))\, \mathrm{d}\tau' \right\} \mathrm{d}\tau. \end{aligned}$$

Hence, equation (22) can be rewritten in terms of the following harmonic kernel:

$$u_{\mathrm{s}}(\mathbf{r}) = -\frac{1}{4\pi\sigma} \int_{\Omega_{\mathrm{c}}} \left[2(\Delta\Psi)(\tau, \theta, \varphi) - \frac{1}{\tau^2} \int_\tau^{c_1} \tau' (\Delta\Psi)(\tau', \theta, \varphi)\, \mathrm{d}\tau' \right] \frac{\mathrm{dV}(\boldsymbol{\tau})}{|\mathbf{r} - \boldsymbol{\tau}|}, \tag{27}$$

$r = d_1$.

2.3 Simultaneous MEG and EEG Measurements

The case of simultaneous MEG and EEG measurements is analyzed in [7]. In this case the basic formulae for EEG are the same, i.e. equations (21), (23) and (24) are still valid. However, for MEG instead of equations (7), (8), (11) and (13), the basic formulae are equations (21) and the following expressions:

$$\frac{4\pi}{\mu} \mathbf{r} \cdot \mathbf{B}(\mathbf{r}) = -\sum_{n=1}^{\infty} \sum_{m=-n}^{n} \frac{c_1^{n+2}}{2n+1} [c_1 \dot{a}_n^m(c_1) - (n-1) a_n^m(c_1)] \frac{Y_n^m(\hat{\mathbf{r}})}{r^{n+1}}, \quad r > d_1, \tag{28}$$

$$A^\tau(\boldsymbol{\tau}) = \sum_{n=1}^{\infty} \sum_{m=-n}^{n} a_n^m(\tau) Y_n^m(\hat{\boldsymbol{\tau}}), \quad 0 < \tau < c_1. \tag{29}$$

The reason for this difference is that now the EEG measurements impose the expansion (21) for the current, thus the expansions (7), (8) are inappropriate.

3 Numerical Implementation

3.1 Description of the Spline Method

For magnetometer measurements, the following data are given

$$b_k = \boldsymbol{\nu}_k \cdot \mathbf{B}(\mathbf{r}_k), \quad k = 1, 2, ..., M, \tag{30}$$

where both $\mathbf{r}_k$ and the unit vector $\boldsymbol{\nu}_k = \boldsymbol{\nu}(\mathbf{r}_k)$ (which is normal to the surface of the device at the point $\mathbf{r}_k$) are known and M is the number of sensors. Our goal is to reconstruct the maximum possible information for the current from the above data. For this purpose, we will use the novel technique of [9, 10] (see also the historical references there), which we now describe. This method (more precisely a version of this method adapted in each case) has already been successfully applied to similar inverse problems in seismic tomography (see [9, 10]) and in inverse gravimetry (see [11, 12]). An enhanced version was used for a combined inversion of seismic and gravitational data (see [13, 14, 15]).

The unique determination of either the function $f_n^m(\tau)$ in equation (11) or the function $a_n^m(\tau)$ of (29) requires some a-priori assumption about the current, such as the assumption that $A^\tau(\boldsymbol{\tau})$ is biharmonic. Thus, we will represent either of these functions in the form $\alpha_n^m G_n(\tau)$, where $G_n(\tau)$ is assumed to be known (in the case of the harmonicity assumption $G_n(\tau)$ is given by τ^n). Hence

$$A^\tau(\boldsymbol{\tau}) = \sum_{n=1}^{\infty} \sum_{j=-n}^{n} \alpha_n^j G_n(\tau) Y_n^j(\hat{\boldsymbol{\tau}}), \quad 0 < \tau < c_1, \tag{31}$$

and similarly for F. This motivates the introduction of the following orthonormal set in $\mathrm{L}^2(\Omega_\mathrm{c})$:

$$H_n^j(\boldsymbol{\tau}) = \gamma_n^{-\frac{1}{2}} G_n(\tau) Y_n^j(\hat{\boldsymbol{\tau}}), \quad \gamma_n = \int_0^{c_1} s^2 G_n^2(s)\, \mathrm{d}s, \quad n \in \mathbb{N}, j = -n, ..., n. \tag{32}$$

The main idea is to expand $A^\tau(\boldsymbol{\tau})$ in terms of appropriate reproducing kernels K [9, 10], instead of spherical harmonics: Let $K(\boldsymbol{\tau}, \mathbf{r})$ be defined by

$$\begin{aligned} K(\boldsymbol{\tau}, \mathbf{r}) &= \sum_{n=1}^{\infty} \sum_{j=-n}^{n} A_n^{-2} H_n^j(\boldsymbol{\tau}) H_n^j(\mathbf{r}) \\ &= \sum_{n=1}^{\infty} \sum_{j=-n}^{n} A_n^{-2} \gamma_n^{-1} G_n(\tau) Y_n^j(\hat{\boldsymbol{\tau}})\, G_n(r) Y_n^j(\hat{\mathbf{r}}), \end{aligned} \tag{33}$$

where the sequence (A_n) has to satisfy a certain summability condition (see [9, 10] for further details).

Let $\mathcal{F}^k$, $k = 1, \ldots, M$, represent the functionals which map A^τ (or F) to the corresponding data $b_k = \boldsymbol{\nu}_k \cdot \mathbf{B}(\mathbf{r}_k)$. In the following we assume that each $\mathcal{F}^k$

is linear and continuous. We use these functionals to construct basis functions for the expansion of A^τ:

$$A^\tau(\boldsymbol{\tau}) = \sum_{k=1}^{M} a_k \mathcal{F}^k_{\mathbf{r}} K(\boldsymbol{\tau}, \mathbf{r}). \tag{34}$$

Here, $\mathcal{F}^k_{\mathbf{r}} K(\boldsymbol{\tau}, \mathbf{r})$ means that $\boldsymbol{\tau}$ is kept fixed and $\mathcal{F}^k$ is applied to the function $\mathbf{r} \mapsto K(\boldsymbol{\tau}, \mathbf{r})$.
In this way we obtain the linear system

$$b_m = \sum_{k=1}^{M} a_k \mathcal{F}^m_{\boldsymbol{\tau}} \mathcal{F}^k_{\mathbf{r}} K(\boldsymbol{\tau}, \mathbf{r}), \tag{35}$$

for the constants a_k, $k = 1, ..., M$.
Mathematical considerations (see [9, 10] and the references therein) show that the reproducing kernel corresponds to a Hilbert space $\mathcal{H}((A_n)) \subset \mathrm{L}^2(\Omega_\mathrm{c})$. This space is equipped with the inner product

$$\langle F, G \rangle_{\mathcal{H}((A_n))} := \sum_{n=1}^{\infty} \sum_{j=-n}^{n} A_n^2 \left\langle F, H_n^j \right\rangle_{\mathrm{L}^2(\Omega_\mathrm{c})} \left\langle G, H_n^j \right\rangle_{\mathrm{L}^2(\Omega_\mathrm{c})}$$

and its induced norm $\| \cdot \|_{\mathcal{H}((A_n))}$. Note that the sequence (A_n^{-1}) is typically chosen to be monotonically decreasing and converging to zero. Thus, this norm provides a kind of non-smoothness measure, since it weights high-degree parts stronger than low-degree parts. Within this context, the following essential features of the method can be established (see [9, 10] and the references therein for proofs):

- If the linear and continuous functionals $\mathcal{F}^k$, $k = 1, ..., M$, are linearly independent, then the linear system (35) is uniquely solvable, i.e. the expansion (34) is unique.
- Among all solutions $F \in \mathcal{H}((A_n))$ satisfying $\mathcal{F}^m F = b_m$, $m = 1, ..., M$, the solution of the form (34) uniquely minimizes the norm $\| \cdot \|_{\mathcal{H}((A_n))}$. Hence, it is the "smoothest" interpolant. This result motivates the name "spline".
- Among all functions of the form (34), the solution given by (35) is closest (in the $\| \cdot \|_{\mathcal{H}((A_n))}$-sense) to the unknown function (best approximation property).

Two further features of the spline method are of particular importance for the numerical implementation.

- The linear system (35) can be regularized by adding a positive constant λ to the diagonal of the matrix. The corresponding spline (34) is then the minimizer of
$$\sum_{k=1}^{M} \left(\mathcal{F}^k A^\tau - b_k \right)^2 + \lambda \left\| A^\tau \right\|^2_{\mathcal{H}((A_n))} .$$

An increased value of λ emphasises the smoothing of the function in relation to the accuracy of the interpolation. Often in practice, a pure interpolation ($\lambda = 0$) is not adequate for a numerical implementation due to the occurence of ill-conditioned matrices (although, for the particular numerical example in this paper, the spline method itself is already a sufficient regularisation of the inverse MEG problem, since the inversion of the unregularised linear system (35) is stable (see Section 3.6); whereas a regularisation of the linear system (35) was necessary for the EEG data).

- The spline (34) can also be represented in terms of a Lagrange basis by

$$A^\tau(\boldsymbol{\tau}) = \sum_{k=1}^{M} b_k \, L_k(\boldsymbol{\tau}), \tag{36}$$

where the Lagrange basis

$$L_k(\boldsymbol{\tau}) = \sum_{j=1}^{M} l_j^{(k)} \, \mathcal{F}_{\mathbf{r}}^j K(\boldsymbol{\tau}, \mathbf{r}), \quad k = 1, \ldots, M,$$

is obtained from the linear systems

$$\sum_{j=1}^{M} l_j^{(k)} \, \mathcal{F}_{\boldsymbol{\tau}}^m \mathcal{F}_{\mathbf{r}}^j K(\boldsymbol{\tau}, \mathbf{r}) = \delta_{mk}, \quad m = 1, \ldots, M, \, k = 1, \ldots M. \tag{37}$$

Note that (37) consists of M linear systems, which all have the same matrix as (35). Equation (37) requires that $\mathcal{F}^m L_k = \delta_{mk}$ such that in (36) $\mathcal{F}^m A^\tau = b_m$, $m = 1, \ldots, M$. This representation in a Lagrange basis is an essential advantage in the case that a time series $\{b_m(t_i)\}_{m=1,\ldots,M,\, i=1,\ldots,N}$ has to be analyzed; indeed, in this case the Lagrange basis is calculated only once and then is stored in the computer. Note that this includes the inversion of the matrix $(\mathcal{F}_{\boldsymbol{\tau}}^m \mathcal{F}_{\mathbf{r}}^j K(\boldsymbol{\tau}, \mathbf{r}))_{m,j=1,\ldots,M}$. The spline can then be calculated almost in real time after the determination of the data b_m, $m = 1, \ldots, M$.

3.2 Details of the Implementation

The implementation of the above scheme using the real magnetometer and electrode information of Elekta Neuromag (R) is discussed below. In this context, we will focus on the determination of F in (11) in terms of $\mathbf{B}$ for the inverse MEG problem.

3.3 The Data Situation

In the following, we assume that the measured magnetic field $\mathbf{B}$ and its potential U are represented in terms of (scalar respectively vector) spherical harmonics by

$$\begin{aligned} U(\mathbf{r}) &= \sum_{n=1}^{\infty} \sum_{j=-n}^{n} c_n^j \, r^{-n-1} Y_n^j\,(\hat{\mathbf{r}})\,, \\ \mathbf{B}(\mathbf{r}) &= \mu \sum_{n=1}^{\infty} \sum_{j=-n}^{n} r^{-n-2}\, c_n^j \left[(-n-1)\,\mathbf{y}_n^{j,1}\,(\hat{\mathbf{r}}) + \sqrt{n(n+1)}\,\mathbf{y}_n^{j,2}\,(\hat{\mathbf{r}})\right], \end{aligned}$$

$|\mathbf{r}| > 1$, where

$$\begin{aligned} \boldsymbol{y}_n^{j,1}\,(\hat{\mathbf{r}}) &:= \hat{\mathbf{r}}\, Y_n^j\,(\hat{\mathbf{r}})\,, \\ \boldsymbol{y}_n^{j,2}\,(\hat{\mathbf{r}}) &:= (n(n+1))^{-1/2}\, \nabla_{\hat{\mathbf{r}}}^{*} Y_n^j\,(\hat{\mathbf{r}})\,. \end{aligned}$$

For further details on the vector spherical harmonics $\boldsymbol{y}_n^{j,i}$ we refer to [8], pp. 321-344. Moreover,

$$F(\boldsymbol{\tau}) = \sum_{n=1}^{\infty} \sum_{j=-n}^{n} F_n^j\, G_n(\tau) Y_n^j(\hat{\boldsymbol{\tau}}). \tag{38}$$

Here, we know due to (13) and (17) that

$$c_n^j = \frac{n}{2n+1} \int_0^{c_1} \tau^{n+1} F_n^j G_n(\tau)\,\mathrm{d}\tau.$$

Based on a-priori conditions, we expect to have a known relation

$$F_n^j = \sigma_n c_n^j; \quad n \in \mathbb{N},\, j = -n, ..., n,$$

with $\sigma_n \neq 0$ for all $n \in \mathbb{N}$. Note that this is a further restriction to the previous assumptions, since we require invertibility ($\sigma_n \neq 0$ for all n), whereas the isotropy (σ_n is independent of j) already follows from the modelling above. The data (see (30)) can then be represented as

$$\begin{aligned} \left(\mathcal{F}^k F =\right) \boldsymbol{\nu}_k \cdot \mathbf{B}(\mathbf{r}_k) &= \mu \sum_{n=1}^{\infty} \sum_{j=-n}^{n} \sigma_n^{-1} F_n^j\, r_k^{-n-2} \left[(-n-1)\boldsymbol{\nu}_k \cdot \mathbf{y}_n^{j,1}\,(\hat{\mathbf{r}}_k)\right. \\ &\qquad \left. + \ \sqrt{n(n+1)}\,\boldsymbol{\nu}_k \cdot \mathbf{y}_n^{j,2}\,(\hat{\mathbf{r}}_k)\right], \end{aligned} \tag{39}$$

where $k = 1, \ldots, 102$. Note that $M = 102$ sensors occur in the case of the considered device.
The considerations for EEG are analogous (see below).

3.4 Spline Basis

We now investigate the practical calculation of the spline basis functions

$$\boldsymbol{\tau} \mapsto \mathcal{F}_{\mathbf{r}}^k K(\boldsymbol{\tau}, \mathbf{r}), \quad k = 1, ..., 102.$$

The use of (39) requires the knowledge of the expansion coefficients F_n^j in (38) if $F(\mathbf{r}) = K(\boldsymbol{\tau}, \mathbf{r})$ for fixed $\boldsymbol{\tau}$. By comparing (33) and (38) we get $F_n^j = A_n^{-2}\gamma_n^{-1} G_n(\tau) Y_n^j(\hat{\boldsymbol{\tau}})$. Hence,

$$\begin{aligned}
\mathcal{F}_{\mathbf{r}}^k K(\boldsymbol{\tau}, \mathbf{r}) = \mu \sum_{n=1}^{\infty} \sum_{j=-n}^{n} & \sigma_n^{-1} A_n^{-2} \gamma_n^{-1} G_n(\tau) Y_n^j\left(\hat{\boldsymbol{\tau}}\right) r_k^{-n-2} \\
& \times \left[(-n-1)\boldsymbol{\nu}_k \cdot \mathbf{y}_n^{j,1}\left(\hat{\mathbf{r}}_k\right) + \sqrt{n(n+1)}\, \boldsymbol{\nu}_k \cdot \mathbf{y}_n^{j,2}\left(\hat{\mathbf{r}}_k\right)\right] \\
= \quad \mu \sum_{n=1}^{\infty} \sigma_n^{-1} A_n^{-2} \gamma_n^{-1} G_n(\tau) r_k^{-n-2} \, \frac{2n+1}{4\pi} & \\
& \times \left[(-n-1)\boldsymbol{\nu}_k \cdot \hat{\mathbf{r}}_k P_n\left(\hat{\boldsymbol{\tau}} \cdot \hat{\mathbf{r}}_k\right) + \boldsymbol{\nu}_k \cdot \left(\hat{\boldsymbol{\tau}} - \left(\hat{\boldsymbol{\tau}} \cdot \hat{\mathbf{r}}_k\right) \hat{\mathbf{r}}_k\right) P_n'\left(\hat{\boldsymbol{\tau}} \cdot \hat{\mathbf{r}}_k\right)\right],
\end{aligned}$$

where the last equation follows from the addition theorem for spherical harmonics.

3.5 Matrix Entries

Before the spline coefficients are available, the system of linear equations has to be solved. For this purpose, the matrix with entries of the form

$$\mathcal{F}_{\boldsymbol{\tau}}^m \mathcal{F}_{\mathbf{r}}^k K(\boldsymbol{\tau}, \mathbf{r}), \quad m, k \in \{1, \ldots, 102\}, \tag{40}$$

has to be computed. They can be calculated as follows:

$$\begin{aligned}
\mathcal{F}_{\boldsymbol{\tau}}^m \mathcal{F}_{\mathbf{r}}^k K(\boldsymbol{\tau}, \mathbf{r}) = \mu^2 \sum_{n=1}^{\infty} \sum_{j=-n}^{n} & \sigma_n^{-2} A_n^{-2} \gamma_n^{-1} r_k^{-n-2} r_m^{-n-2} \\
& \times \left[(-n-1)\boldsymbol{\nu}_k \cdot \mathbf{y}_n^{j,1}\left(\hat{\mathbf{r}}_k\right) + \sqrt{n(n+1)}\, \boldsymbol{\nu}_k \cdot \mathbf{y}_n^{j,2}\left(\hat{\mathbf{r}}_k\right)\right] \\
& \times \left[(-n-1)\boldsymbol{\nu}_m \cdot \mathbf{y}_n^{j,1}\left(\hat{\mathbf{r}}_m\right) + \sqrt{n(n+1)}\, \boldsymbol{\nu}_m \cdot \mathbf{y}_n^{j,2}\left(\hat{\mathbf{r}}_m\right)\right] \\
= \quad & \mu^2 \sum_{n=1}^{\infty} \sigma_n^{-2} A_n^{-2} \gamma_n^{-1} \left(r_k r_m\right)^{-n-2} \, \frac{2n+1}{4\pi} \\
& \times \Big[(-n-1)^2 \left(\boldsymbol{\nu}_k \cdot \hat{\mathbf{r}}_k\right) \left(\boldsymbol{\nu}_m \cdot \hat{\mathbf{r}}_m\right) P_n\left(\hat{\mathbf{r}}_k \cdot \hat{\mathbf{r}}_m\right) \\
& +(-n-1) \left(\left(\boldsymbol{\nu}_m \cdot \hat{\mathbf{r}}_m\right) \boldsymbol{\nu}_k \cdot \nabla_\xi^* + \left(\boldsymbol{\nu}_k \cdot \hat{\mathbf{r}}_k\right) \boldsymbol{\nu}_m \cdot \nabla_\eta^*\right) P_n(\boldsymbol{\xi} \cdot \boldsymbol{\eta})\Big|_{\boldsymbol{\xi}=\hat{\mathbf{r}}_k, \boldsymbol{\eta}=\hat{\mathbf{r}}_m} \\
& + \boldsymbol{\nu}_k^{\mathrm{T}} \left(\nabla_{\boldsymbol{\xi}}^* \otimes \nabla_{\boldsymbol{\eta}}^* P_n(\boldsymbol{\xi} \cdot \boldsymbol{\eta})\right) \boldsymbol{\nu}_m \Big|_{\boldsymbol{\xi}=\hat{\mathbf{r}}_k, \boldsymbol{\eta}=\hat{\mathbf{r}}_m}\Big] \\
= \quad & \mu^2 \sum_{n=1}^{\infty} \sigma_n^{-2} A_n^{-2} \gamma_n^{-1} \left(r_k r_m\right)^{-n-2} \, \frac{2n+1}{4\pi} \\
& \times \left[(-n-1)^2 \left(\boldsymbol{\nu}_k \cdot \hat{\mathbf{r}}_k\right) \left(\boldsymbol{\nu}_m \cdot \hat{\mathbf{r}}_m\right) P_n\left(\hat{\mathbf{r}}_k \cdot \hat{\mathbf{r}}_m\right) \right. \\
& +(-n-1) \left(\left(\boldsymbol{\nu}_m \cdot \hat{\mathbf{r}}_m\right) \left(\boldsymbol{\nu}_k \cdot f\left(\hat{\mathbf{r}}_k, \hat{\mathbf{r}}_m\right)\right)\right.
\end{aligned}$$

$$
\begin{aligned}
&+ (\boldsymbol{\nu}_k \cdot \hat{\mathbf{r}}_k) (\boldsymbol{\nu}_m \cdot f(\hat{\mathbf{r}}_m, \hat{\mathbf{r}}_k))) P_n'(\hat{\mathbf{r}}_k \cdot \hat{\mathbf{r}}_m) \\
&+ (\boldsymbol{\nu}_k \cdot f(\hat{\mathbf{r}}_k, \hat{\mathbf{r}}_m)) (f(\hat{\mathbf{r}}_m, \hat{\mathbf{r}}_k) \cdot \boldsymbol{\nu}_m) P_n''(\hat{\mathbf{r}}_k \cdot \hat{\mathbf{r}}_m) \\
&+ \boldsymbol{\nu}_k^{\mathrm{T}} g(\hat{\mathbf{r}}_k, \hat{\mathbf{r}}_m) \boldsymbol{\nu}_m P_n'(\hat{\mathbf{r}}_k \cdot \hat{\mathbf{r}}_m)\big],
\end{aligned}
$$

where $f(\boldsymbol{\xi}, \boldsymbol{\eta}) := \nabla^*_{\boldsymbol{\xi}}(\boldsymbol{\xi} \cdot \boldsymbol{\eta}) = \boldsymbol{\eta} - (\boldsymbol{\xi} \cdot \boldsymbol{\eta})\boldsymbol{\xi}$ for $\boldsymbol{\xi}, \boldsymbol{\eta} \in \Omega$,

$$
g(\boldsymbol{\xi}, \boldsymbol{\eta}) := \nabla^*_{\boldsymbol{\xi}} \otimes (\boldsymbol{\xi} - (\boldsymbol{\eta} \cdot \boldsymbol{\xi})\boldsymbol{\eta}) = \mathbb{1} - \boldsymbol{\xi} \otimes \boldsymbol{\xi} - (\boldsymbol{\eta} - (\boldsymbol{\xi} \cdot \boldsymbol{\eta})\boldsymbol{\xi}) \otimes \boldsymbol{\eta},
$$

$\mathbb{1}$ is the 3×3 - identity matrix and ∇^* is the surface gradient with respect to the unit sphere Ω. The derived expansion in Legendre polynomials can (in a truncated form) be numerically evaluated by the use of the Clenshaw algorithm (see [16]).

3.6 A Numerical Example for MEG

We will study here the case where F is restricted to a spherical shell given by $0 < a \leq \tau \leq 1 < c_1$. Moreover, we assume that the density F has a vanishing zeroth moment (i.e. its zeroth degree coefficient vanishes) and only depends on the angular variables but not on the radial one. For this purpose we can easily derive a spectral relation between U, F, and $\mathbf{B}$ by using the results above.

Theorem 3.1 *Let $0 < a < 1 < c_1$ be a given real number. Furthermore, let $F : \Omega_{\mathrm{c}} \to \mathbb{R}$ be a given function which is square–integrable and satisfies (11), (12) and the following conditions:*

$$
\begin{aligned}
\int_\Omega F(\boldsymbol{\tau}) \, \mathrm{dS}(\hat{\boldsymbol{\tau}}) &= 0 \textit{ for all } \tau \in [0, c_1], &(41)\\
F(\boldsymbol{\tau}) &= 0 \textit{ if } \tau \notin [a, 1], &(42)\\
F(\boldsymbol{\tau}) &= F(\mathbf{r}) \textit{ if } \hat{\boldsymbol{\tau}} = \hat{\mathbf{r}} \textit{ and } \tau, r \in [a, 1]. &(43)
\end{aligned}
$$

Then the corresponding function $U \in \mathrm{L}^2(\Omega_{\mathrm{e}})$ is given by

$$
U(\mathbf{r}) = \sum_{n=1}^{\infty} \sum_{m=-n}^{n} c_n^m r^{-n-1} Y_n^m(\hat{\mathbf{r}}), \quad \mathbf{r} \in \Omega_{\mathrm{e}}. \tag{44}
$$

with

$$
f_n^m(\tau) = \underbrace{\frac{n+2}{1 - a^{n+2}} \, \frac{2n+1}{n}}_{=\sigma_n} c_n^m, \quad \tau \in [a, 1]
$$

The convergence of the series in (44) has to be understood in the sense of $\mathrm{L}^2(\Omega_{\mathrm{c}})$.

Proof. From Theorem 2.1 we know that $F \in \mathrm{L}^2(\Omega_{\mathrm{c}})$ with

$$
F(\boldsymbol{\tau}) = \sum_{n=1}^{\infty} \sum_{m=-n}^{n} f_n^m(\tau) Y_n^m(\hat{\boldsymbol{\tau}})
$$

and (12) (note that condition (41) implies that the coefficient for $n = 0$ vanishes) is related to U by

$$\int_0^{c_1} \tau^{n+1} f_n^m(\tau) d\tau = \frac{2n+1}{n}\, c_n^m; \quad n = 1, 2, ...;\ m = -n, ..., n.$$

Due to the assumptions (42) and (43) on F, i.e. $f_n^m(\tau) = F_n^m$ if $\tau \in [a, 1]$ and $= 0$ else, we conclude that

$$\begin{aligned} \int_a^1 \tau^{n+1}\, \mathrm{d}\tau\, F_n^m &= \frac{2n+1}{n}\, c_n^m \\ \Leftrightarrow F_n^m &= \frac{n+2}{1-a^{n+2}}\, \frac{2n+1}{n}\, c_n^m \ . \end{aligned}$$

■

Hence, in this particular case we have

$$\begin{aligned} \sigma_n &= \frac{n+2}{1-a^{n+2}}\, \frac{2n+1}{n}, \\ G_n(\tau) &= \chi_{[a,1]}(\tau), \qquad\qquad (45) \\ \gamma_n &= \int_0^{c_1} s^2 G_n^2(s)\, \mathrm{d}s = \int_a^1 s^2\, \mathrm{d}s = \frac{1}{3}\left(1 - a^3\right). \end{aligned}$$

Note that the associated functionals $\mathcal{F}^k$ (see (39)) are obviously linear. Moreover, the norm of F is given by

$$\|F\|^2_{\mathrm{L}^2(\Omega_c)} = \sum_{n=1}^{\infty} \sum_{j=-n}^{n} \left(F_n^j\right)^2 \gamma_n$$

and the triangle inequality as well as the Cauchy–Schwarz inequality yield the following estimate:

$$\begin{aligned} \left|\mathcal{F}^k F\right| &\leq \mu \sum_{n=1}^{\infty} \sum_{j=-n}^{n} \sigma_n^{-1} \left|F_n^j\right| r_k^{-n-2} \left[(n+1)\sqrt{\frac{2n+1}{4\pi}} + \sqrt{n(n+1)}\sqrt{\frac{2n+1}{4\pi}}\right] \\ &\leq \frac{\mu}{\sqrt{4\pi}} \left(\sum_{n=1}^{\infty} \sum_{j=-n}^{n} \left(F_n^j\right)^2 \gamma_n\right)^{1/2} \\ &\quad \times \left(\sum_{n=1}^{\infty} \sum_{j=-n}^{n} \gamma_n^{-1} \sigma_n^{-2} r_k^{-2n-4} 4(n+1)^2(2n+1)\right)^{1/2} \\ &\leq \frac{\mu}{\sqrt{\pi}} \|F\|_{\mathrm{L}^2(\Omega_c)} \left(\sum_{n=1}^{\infty} \sum_{j=-n}^{n} \gamma_n^{-1} \sigma_n^{-2} r_k^{-2n-4} (2n+1)^3\right)^{1/2} . \end{aligned}$$

Hence, each functional $\mathcal{F}^k$ is continuous, since the latter series converges (note that $|r_k| > 1$).

In the numerical test, we use the following example: F is the sum of two kernels of the following form:

$$\boldsymbol{\tau} \mapsto \kappa \, \frac{1}{4\pi} \, \frac{1-h^2}{\left(1+h^2-2h\,(\boldsymbol{\eta}\cdot\hat{\boldsymbol{\tau}})\right)^{3/2}} - \frac{1}{4\pi} = \kappa \sum_{l=1}^{\infty} \frac{2l+1}{4\pi} \, h^l P_l\left(\boldsymbol{\eta}\cdot\hat{\boldsymbol{\tau}}\right) \quad ,$$

where $\kappa \in \mathbb{R}$, $h \in]-1,1[$, and $\boldsymbol{\eta} \in \Omega$ are fixed. Here, we choose $\kappa_1 = 0.029$, $h_1 = 0.7$, and $\boldsymbol{\eta}^{(1)} = (1,1,1)/\sqrt{3}$ for the first kernel and $\kappa_2 = 0.0047$, $h_2 = 0.8$, and $\boldsymbol{\eta}^{(2)} = (-1,0,1)/\sqrt{2}$ for the second one.
In other words, we have

$$F_n^j = \sum_{i=1}^{2} \kappa_i \, h_i^n \, Y_n^j\left(\boldsymbol{\eta}^{(i)}\right) \tag{46}$$

in (38). Figure 1 shows F on the upper hemisphere.

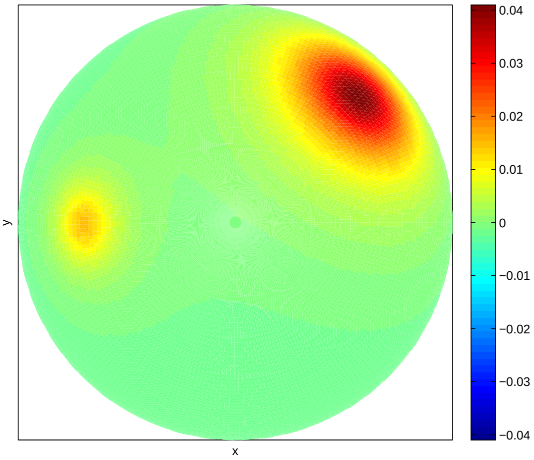

Figure 1: Exact solution F of the numerical MEG test

By inserting (46) in (39) we obtain

$$\begin{aligned} \boldsymbol{\nu}_k \cdot \mathbf{B}\left(\mathbf{r}_k\right) \quad = \quad & \mu \sum_{i=1}^{2} \kappa_i \sum_{n=1}^{\infty} \sigma_n^{-1} h_i^n r_k^{-n-2} \frac{2n+1}{4\pi} \left[(-n-1)\boldsymbol{\nu}_k \cdot \hat{\mathbf{r}}_k \, P_n\left(\boldsymbol{\eta}^{(i)} \cdot \hat{\mathbf{r}}_k\right)\right. \\ & \left. + \boldsymbol{\nu}_k \cdot \left(\boldsymbol{\eta}^{(i)} - \left(\hat{\mathbf{r}}_k \cdot \boldsymbol{\eta}^{(i)}\right)\hat{\mathbf{r}}_k\right) \, P_n'\left(\boldsymbol{\eta}^{(i)} \cdot \hat{\mathbf{r}}_k\right)\right] \end{aligned}$$

Since a closed representation of this series is unknown to us, we truncate the summation at degree 1000 and use this approximation for the given data (we,

correspondingly, also truncate the exact solution at this degree), where $a = 0.9$. Moreover, we used the real sensor positions $\mathbf{r}_k$ and normal vectors $\boldsymbol{\nu}_k$ of Elekta Neuromag (R), where the radii r_k of the sensor positions $\mathbf{r}_k$ range from 1.0635 to 1.4571.
The Lagrange basis (with $A_n = 0.75^{-n/2}$ in the reproducing kernel and truncation of the corresponding series at degree 100) was calculated where the inversion of the matrix was stable enough such that no regularisation was necessary. Figure 2 shows the matrix.

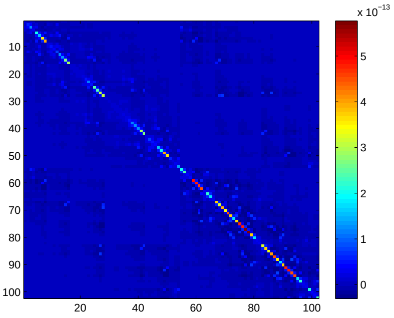

Figure 2: Matrix for the determination of the Lagrange basis

Figure 3 shows the resulting spline and the errors with respect to F for different noise levels. Note that the colorbars for the exact solution and the splines are set in the same way for reasons of a better comparison. With respect to a point grid $\{\boldsymbol{x}_i\}_{i=1,\ldots,14,400}$ on the upper hemisphere (the grid used for the plotting in Figure 3) the RMS error

$$\left(\frac{1}{14,400}\sum_{i=1}^{14,400}\left(\sum_{k=1}^{102}\boldsymbol{\nu}_k\cdot\mathbf{B}\left(\mathbf{r}_k\right)\,L_k\left(\boldsymbol{x}_i\right)-F\left(\boldsymbol{x}_i\right)\right)^2\right)^{\frac{1}{2}}$$

is shown in Table 1. Note that $\max_{1\le i\le 14,400}|F(\boldsymbol{x}_i)| \approx 0.041$. The results show that a close and stable approximation can be obtained via the described numerical method.

We compare the results with the solution obtained via a spherical harmonics expansion. For this purpose, we use the ansatz (38) with the parameters (45). The corresponding system of linear equations is represented by (39). For the numerical implementation, the fully normalized spherical harmonics were used. For calculating the vector spherical harmonics, well known formulae for the derivatives of the associated Legendre functions were used (see [17, pp 79-82] for further details).

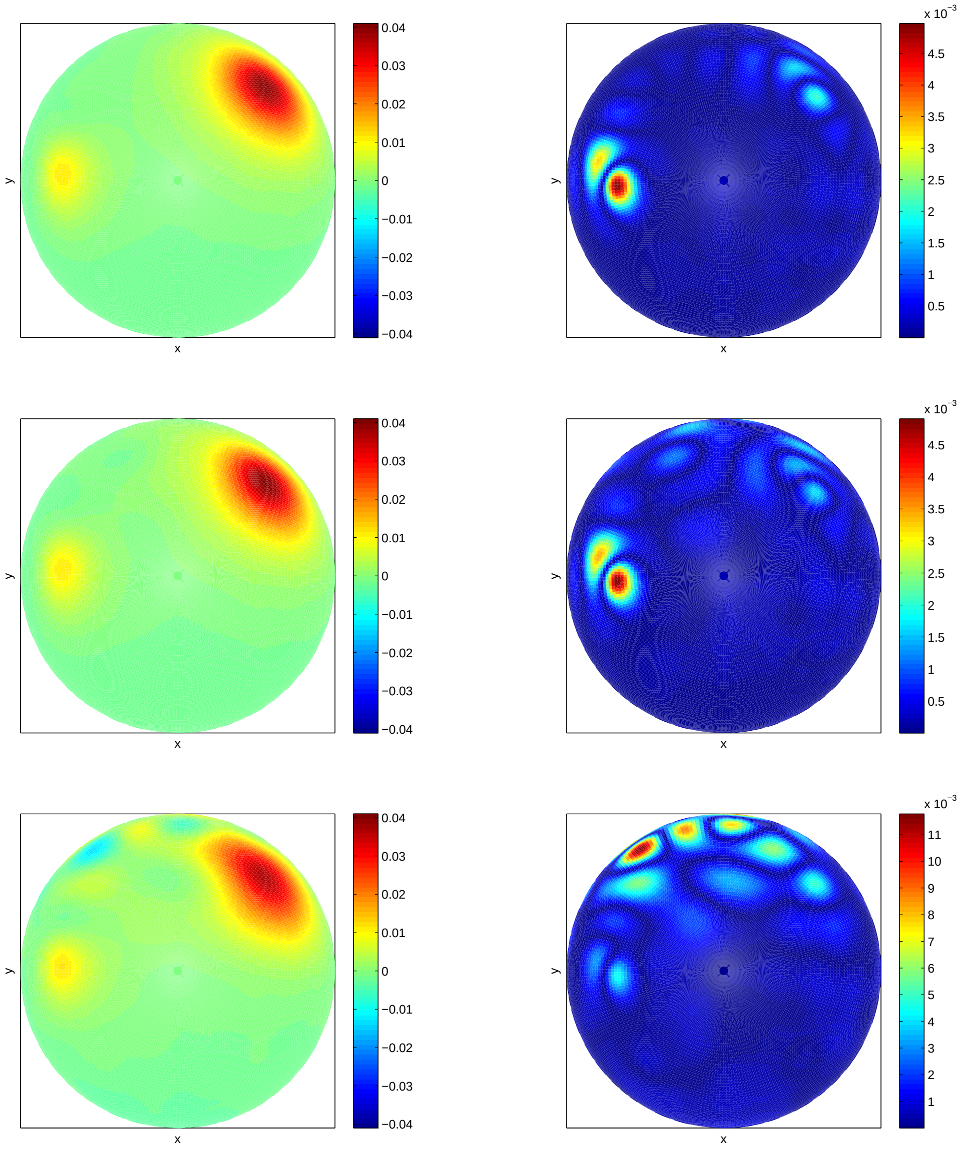

Figure 3: Spline (left hand column) and absolute error (right hand column) for different levels of noise: Each data $\boldsymbol{\nu}_k \cdot \mathbf{B}(\mathbf{r}_k)$ was disturbed by a random number in the range $[-p\%, p\%] \cdot \max_k(\boldsymbol{\nu}_k \cdot \mathbf{B}(\mathbf{r}_k))$ for $p = 0$ (1^{st} row), $p = 1$ (2^{nd} row) and $p = 5$ (3^{rd} row).

Level of noise	RMS error spline	RMS error spherical harmonics
0	0.00032771	0.0024803
1	0.00033934	0.0024919
5	0.0011438	0.0025557

Table 1: RMS error with respect to the level of noise (in % of the maximum data value $\boldsymbol{\nu}_k \cdot \mathbf{B}(\mathbf{r}_k)$) in case of the spline approximation (2nd column) and the spherical harmonics approximation (3rd column) for the synthetic MEG example

We use the maximal degree 9 such that the number of unknowns, which is in the case of this choice 99, does not exceed the number of equations, which is here 102. Due to the non-quadratic system "$Ax = b$", we use the normal equation "$A^{\mathrm{T}}Ax = A^{\mathrm{T}}b$". Since the matrix $A^{\mathrm{T}}A$ is numerically singular, we add a regularisation parameter to the diagonal and this parameter was chosen based on the L-curve method (see Figure 4). The results are illustrated in Figure 5. The corresponding RMS errors are listed in Table 1.

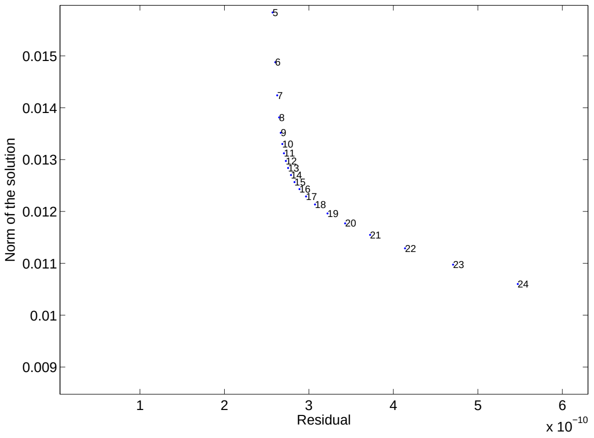

Figure 4: L-curve for the normal equation: the norm of the approximate solution "$\|x\|$" is plotted against the residual "$\|Ax-b\|$". The parameters $\lambda_k = 10^{-4+\frac{k-1}{8}} \cdot \max_{i,j} |a_{i,j}|$ were compared. The L-curves for the considered noise levels all look rather similar such that only the curve for 1% noise is shown here. In each case, λ_{17} was chosen. The numbers in the graph refer to the index k of λ_k.

The results show that the error is obviously smaller for the spline approximation in comparison to the spherical harmonics expansion. On the other hand, the error is more sensitive to the noise in the case of the spline. However, the error

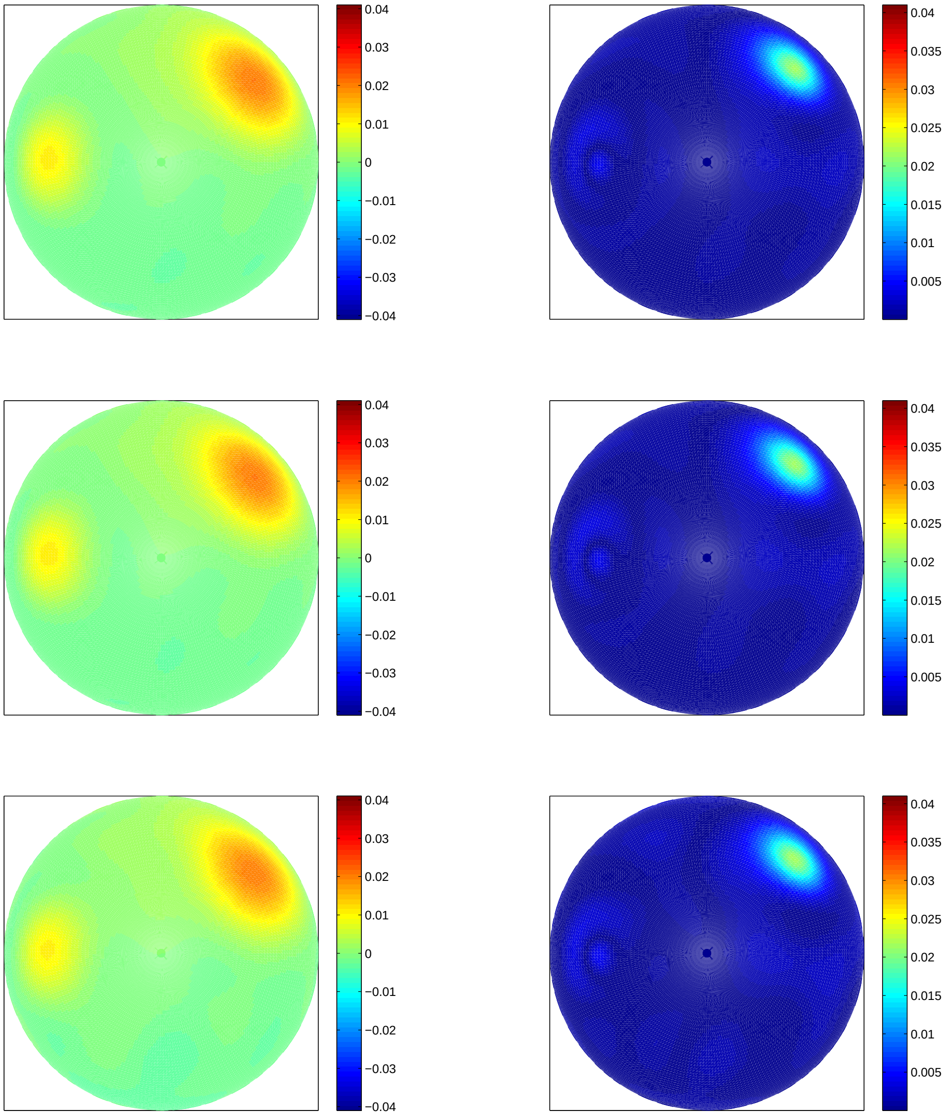

Figure 5: Spherical harmonics based approximation (left-hand column) and absolute error (right-hand column) for different levels of noise. The same data as in Figure 3 were used. The noise levels again range from 0% (top) to 5% (bottom).

for the spline in the case of 5% noise is still significantly smaller than the error for the spherical harmonics expansion.

3.7 A Numerical Example for EEG

Here, the radii of the 70 data points vary from 0.8702 to 1.5247. The approximating spline is shown at a hemisphere with the radius 0.6. A minimal norm solution was chosen as a uniqueness constraint. The corresponding formulae are as follows: Based on (25), $u_{\mathrm{s}}(\boldsymbol{r})$ is representable as

$$u_{\mathrm{s}}(\boldsymbol{r}) = \sum_{n=1}^{\infty} \sum_{m=-n}^{n} u_n^m \left(\frac{d_1}{r}\right)^{n+1} Y_n^m(\hat{\boldsymbol{r}}), \tag{47}$$

where the unknown function is

$$\Psi(\boldsymbol{\tau}) = \sum_{n=1}^{\infty} \sum_{m=-n}^{n} \frac{u_n^m}{s_n} \left(\ln \tau - \frac{1}{n}\right) \tau^n Y_n^m(\hat{\boldsymbol{\tau}})$$

(see [19]). In the notation of Sections 3.1 and 3.3, we have

$$\begin{aligned}
G_n(\tau) &= \left(\ln \tau - \frac{1}{n}\right) \tau^n, \\
\gamma_n &= \int_0^{c_1} s^2 \left(\ln s - \frac{1}{n}\right)^2 s^{2n}\, \mathrm{d}s \\
&= \frac{c_1^{2n+3}}{2n+3} \left(\ln^2 c_1 - \frac{2 \ln c_1}{2n+3} + \frac{2}{(2n+3)^2} - \frac{2 \ln c_1}{n} + \frac{2}{n(2n+3)} + \frac{1}{n^2}\right) \\
c_n^m &= u_n^m d_1^{n+1}, \\
F_n^m &= \frac{u_n^m}{s_n}, \\
\sigma_n &= \frac{1}{s_n d_1^{n+1}}.
\end{aligned}$$

For the numerical implementation, the constants s_n were obtained via the system of linear equations (26)-(32) in [18] with $c_1 = 0.71\,\mathrm{dm}$, $f_1 = 0.72\,\mathrm{dm}$, $b_1 = 0.79\,\mathrm{dm}$, $d_1 = 0.85\,\mathrm{dm}$, $\sigma_{\mathrm{c}} = 0.033\,\frac{\mathrm{S}}{\mathrm{dm}}$, $\sigma_{\mathrm{f}} = 0.1\,\frac{\mathrm{S}}{\mathrm{dm}}$, $\sigma_{\mathrm{b}} = 0.0042\,\frac{\mathrm{S}}{\mathrm{dm}}$, and $\sigma_{\mathrm{d}} = 0.033\,\frac{\mathrm{S}}{\mathrm{dm}}$. The corresponding matrix was regularized by adding 10% of the absolutely maximal entry to the diagonal (the value 10% is a trial-and-error value).

The given data have the form

$$u_{\mathrm{s}}(\boldsymbol{r}_k), \quad k = 1, \ldots, N.$$

The corresponding spline basis functions are, consequently,

$$\begin{aligned}
\mathcal{F}^k_{\boldsymbol{r}} K(\boldsymbol{\tau},\boldsymbol{r}) &= \sum_{\substack{n=1\\ s_n\neq 0}}^{\infty} \sum_{j=-n}^{n} \sigma_n^{-1} A_n^{-2} \gamma_n^{-1} G_n(\tau) r_k^{-n-1} Y_n^j(\hat{\boldsymbol{\tau}}) Y_n^j(\hat{\boldsymbol{r}}_k) \\
&= \sum_{\substack{n=1\\ s_n\neq 0}}^{\infty} \sigma_n^{-1} A_n^{-2} \gamma_n^{-1} G_n(\tau) r_k^{-n-1} \, \frac{2n+1}{4\pi} \, P_n\left(\hat{\boldsymbol{\tau}} \cdot \hat{\boldsymbol{r}}_k\right)
\end{aligned}$$

and the associated matrix entries are

$$\begin{aligned}
\mathcal{F}^m_{\boldsymbol{\tau}} \mathcal{F}^k_{\boldsymbol{r}} K(\boldsymbol{\tau},\boldsymbol{r}) &= \sum_{\substack{n=1\\ s_n\neq 0}}^{\infty} \sum_{j=-n}^{n} \sigma_n^{-2} A_n^{-2} \gamma_n^{-1} r_k^{-n-1} Y_n^j(\hat{\boldsymbol{r}}_k) r_m^{-n-1} Y_n^j(\hat{\boldsymbol{r}}_m) \\
&= \sum_{\substack{n=1\\ s_n\neq 0}}^{\infty} \sigma_n^{-2} A_n^{-2} \gamma_n^{-1} \left(r_k r_m\right)^{-n-1} \, \frac{2n+1}{4\pi} \, P_n\left(\hat{\boldsymbol{r}}_k \cdot \hat{\boldsymbol{r}}_m\right).
\end{aligned}$$

The chosen sequence is $A_n = h^{n(n+1)/2}$ with $h = 0.99$.
It turns out that the matrix is numerically singular but already very small values added to the diagonal yield a satisfactory regularisation. The corresponding L-curve (see Figure 6) does not provide us with a proper "L". We chose $\lambda \approx 1.78 \cdot 10^{-13}$ multiplied with the absolute maximum of the matrix entries as the regularisation parameter.

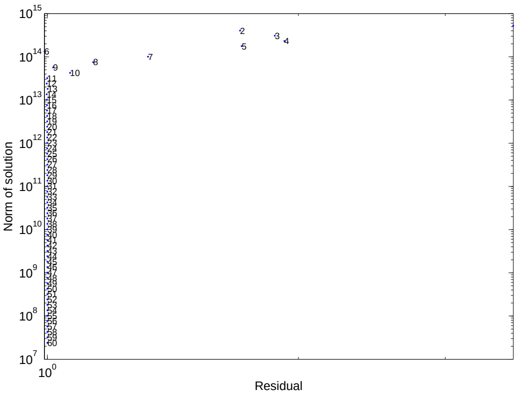

Figure 6: L-curve for the matrix inversion corresponding to the Lagrange basis for EEG: the norm of the inverse matrix "$\|A^{-1}\|$"is plotted against the residual "$\|A^{-1}A-I\|$", where I is the identity matrix. The parameters $\lambda_k = 10^{-14+\frac{k-1}{8}} \cdot \max_{i,j} |a_{i,j}|$ were compared and λ_{11} was chosen. The numbers in the graph refer to the index k of λ_k.

For a synthetic verification test, we use

$$\Psi(\boldsymbol{\tau}) = \sum_{i=1}^{2} \kappa_i \sum_{l=1}^{1000} h_i^l \left(\frac{\tau}{d_1}\right)^l \left(\ln\tau - \frac{1}{l}\right) \frac{2l+1}{4\pi} P_l\left(\eta^{(i)} \cdot \hat{\boldsymbol{\tau}}\right)$$

as the unknown (time-independent) function and $\boldsymbol{A} \equiv 0$. This corresponds to the given electric potential

$$u_{\mathrm{s}}(\boldsymbol{r}) = \sum_{i=1}^{2} \kappa_i \sum_{n=1}^{1000} s_n \left(\frac{h_i}{d_1}\right)^n \left(\frac{d_1}{r}\right)^{n+1} \frac{2n+1}{4\pi} P_n\left(\eta^{(i)} \cdot \hat{\boldsymbol{r}}\right).$$

We chose $\kappa_1 = 0.029$, $\kappa_2 = 0.015$, $h_1 = 0.8$, $h_2 = 0.9$, $\eta^{(1)} = (1,1,1)/\sqrt{3}$, and $\eta^{(2)} = (-1,0,1)/\sqrt{2}$ (see Figure 7 for the exact solution). Again (as it was the case for MEG), the real sensor positions were used for the synthetic data. Figure 8 and Table 2 show the results of a spline reconstruction. Note that the colorbars for the exact solution and the spline are set in the same way for reasons of a better comparison.

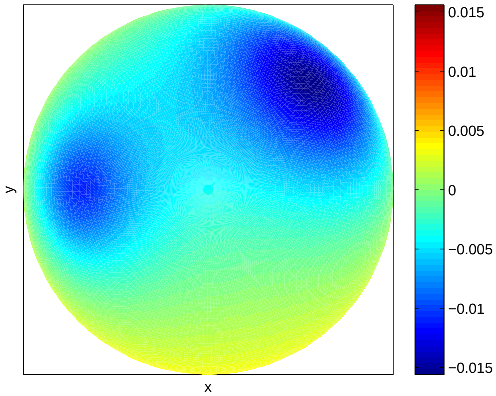

Figure 7: Exact solution Ψ of the synthetic EEG example

RMS error spline	RMS error spherical harmonics
0.00034411	0.59852

Table 2: RMS error in case of the spline approximation and the spherical harmonics approximation for the synthetic EEG example

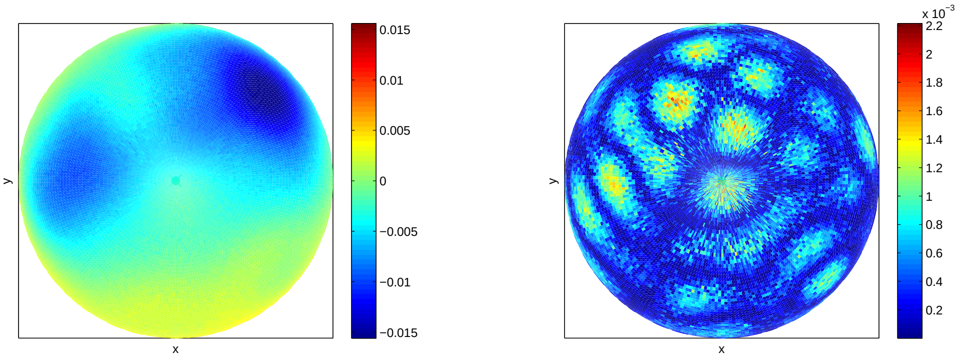

Figure 8: Spline (left-hand) and absolute error for the synthetic EEG example

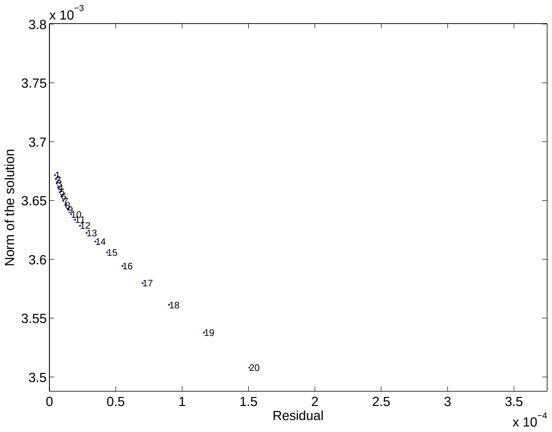

Figure 9: L-curve (norm of the solution vector in comparison to the norm of the residual) for the spherical harmonics approach in case of the EEG inversion: The parameters $\lambda_k = 10^{-4+\frac{k-1}{8}} \cdot \max_{i,j} |a_{i,j}|$ were compared and λ_{11} was chosen. The numbers in the graph refer to the index k of λ_k.

The more serious instability of the EEG inversion also influences the results for a spherical harmonics approach. We use (47) to determine the expansion coefficients u_n^m. This yields a system of linear equations with the potential data as the given right-hand side. The regularisation parameter is chosen via the L-curve method (see Figure 9). The maximal degree is 7 such that 63 expansion coefficients are determined. The obtained results (Figure 10 and Table 2) show that spherical harmonics are not appropriate for this kind of problem. The instability of the problem in combination with the inhomogeneity of the point

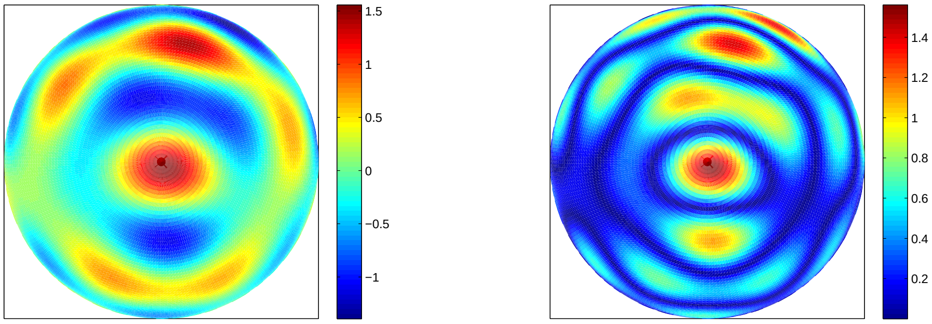

Figure 10: Spherical harmonics approximation (left-hand) and absolute error for the synthetic EEG example

grid probably cause this effect.

These results show that the use of the described spline method appears to be a reasonable alternative to present approaches for both inverse MEG and inverse EEG.

4 Conclusions

The basic inverse problems for the functional imaging techniques of MEG and EEG consist of estimating the neuronal current $\boldsymbol{J}^{\mathrm{P}}(\boldsymbol{\tau}), \boldsymbol{\tau} \in \Omega_{\mathrm{c}}$ in terms of the electric potential $u_{\mathrm{s}}(\boldsymbol{r}), \boldsymbol{r} \in \partial\Omega_{\mathrm{d}}$, and of the quantity $\boldsymbol{\nu} \cdot \boldsymbol{B}(\boldsymbol{r}), \boldsymbol{r} \in \Omega_{\mathrm{e}}$, respectively, where Ω_{c} denotes the space occupied by the cerebrum, $\partial\Omega_{\mathrm{d}}$ denotes the scalp, Ω_{e} denotes the space exterior to the head, $\boldsymbol{B}(\boldsymbol{r})$ denotes the magnetic field and $\boldsymbol{\nu}$ is a certain unit vector. For the three-shell spherical model, an explicit formula for $\boldsymbol{J}^{\mathrm{P}}$ in the case of simultaneous MEG and EEG measurements was derived in [7]. Here, we have presented the rigorous derivation of $\boldsymbol{J}^{\mathrm{P}}$ in terms of $u_{\mathrm{s}}(\boldsymbol{r})$ and of $\boldsymbol{\nu} \cdot \boldsymbol{B}(\boldsymbol{r})$, for the case of independent as well as simultaneous EEG and MEG measurements. Furthermore, we have presented a novel numerical implementation of the analytical formulae based on the reproducing kernel technique of [10] and [11].

In the case of independent MEG measurements the relevant formula is identical to that derived in [3] and [18], but now the derivation is both rigorous and simpler. The formulae (13) and (24) show that MEG and EEG measurements yield information about two of the three scalar functions specifying the neuronal current. In particular, it is possible to determine the angular parts of these two functions as well as to obtain explicit constraints satisfied by their radial parts. The complete determination of the radial parts of these two functions, as well as the determination of the third scalar function specifying the current, requires some additional *a priori* assumptions about the current. One such assumption is that the current minimises the L^2-norm. In this case for independent MEG and EEG measurements, the radial parts of the functions $f_n^m(\tau)$ and $\psi_n^m(\tau)$ are proportional to τ^{m+1} and $(\ln\tau - \frac{1}{n})\tau^n$ respectively (see [19]). The derivation of the corresponding formulae in the case of simultaneous MEG and EEG data is presented in [19].

Our plan in the future is to compare our approach with commercial software using anthropomorphic data. We will use independent as well as simultaneous MEG and EEG measurements and also, in order to obtain a unique current, we will use L^2-minimization, as well as other types of constraints.

Regarding other approaches to reconstructing the neuronal current, we note that existing strategies can be divided into two broad categories [20]: those based on dipole models and those based on continuously distributed models. Our approach assumes a continuously distributed current, thus in what follows we discuss only the latter models. The most well known such approach is the minimum norm solution which assumes that the three-dimensional current distributions should have minimum L^2-norm (see [21, 22]). This approach differs from our approach since we *first* identify the part of the current that can be determined from the measurements, and *then* we minimize the relevant L^2-norm. This yields an *explicit analytic formula*. Similar remarks are valid for the other weighted minimum norm approaches used in the literature, such as FOCUSS [23] and RWMN [24], as well as for the Laplacian weighted minimum norm approach called LORETA [25].

In the case of independent EEG measurements, our approach provides the analytical solution, as well as the numerical implementation, of the so-called ELECTRA model [26]; the advantage of this model is that it can be compared with intracranial recordings.

It appears that the main advantages of our approach are the following: (a) it can indentify precisely the part of the neuronal current that can be determined from the given measurements; (b) it has the flexibility to be supplemented with any regularisation strategy such as L^2-minimization and the minimizations used in FOCUSS, RWMN and LORETA; (c) it can be numerically implemented in an effective, stable way. However, it should be emphasised that until the method is applied to real data and is compared with commercial software, the above advantages are purely speculative.

An important limitation of our approach is the assumption of a *spherical* model. We envision to overcome this limitation as follows: (a) to attempt the numerical implementation of the formulae of [7] associated with the three-shell ellipsoidal model; (b) to implement the overlapping sphere head model, proposed in [27]; (c) to implement the spherical head model with anatomical constraints [28]. Progress in this direction will be reported in future publications.

Finally, we note that Elekta Neuromag (R) in addition to measuring $\boldsymbol{\nu}(\boldsymbol{r})\cdot\boldsymbol{B}(\boldsymbol{r})$, it also measures $\nabla_{\hat{\boldsymbol{r}}}(\boldsymbol{\nu}(\boldsymbol{r})\cdot\boldsymbol{B}(\boldsymbol{r}))$. These latter data can also be handled using the numerical technique of Section 3. The question of extracting further information for the current from these additional data is under investigation.

Acknowledgments

This work was partially supported by the EPSRC and the German Research Foundation (DFG, project MI 655/4-1). Olaf Hauk acknowledges support from the MRC UK (MC_US_A060_0050). Furthermore, Volker Michel gratefully acknowledges the hospitality of the Isaac Newton Institute for Mathematical Sciences, Cambridge, UK and the Department of Applied Mathematics and Theoretical Physics of the University of Cambridge.

References

[1] D.B. Geselowitz: On Bioelectric Potentials in an Inhomogeneous Volume Conductor, Biophysical Journal, **7**, 1-11, (1967).

[2] J. Sarvas: Basic Mathematical and Electromagnetic Concepts of the Biomagnetic Inverse Problem, Physics in Medicine and Biology, **32**, 11-22, (1987).

[3] A.S. Fokas, I.M. Gelfand and Y. Kurylev: Inversion Method for magnetoencephalography, Inverse Problems, **12**, L9-L11, (1996).

[4] A.S. Fokas, Y. Kurylev and V. Marinakis: The Unique Determination of Neuronal Current in the Brain Via Magnetoencephalography, Inverse Problems, **20**, 1067-1087, (2004).

[5] G. Dassios, A.S. Fokas and F. Kariotou: On the Non-Uniqueness of the Inverse MEG Problem, Inverse Problems, **21**, L1-L5 (2005).

[6] G. Dassios, A.S. Fokas and D. Hadjiloizi: On the Complementarity of Electroencephalography and Magnetoencephalography, Inverse Problems, **23**, 2541-2549, (2007).

[7] A.S. Fokas: Electro-Magneto-Encephalography for the three-Shell Model: Distributed Current in Arbitrary, Spherical and Ellipsoidal Geometries, J. R. Soc. Interface, doi:10.1098/rsif.2008.0309, (2008).

[8] W. Freeden, T. Gervens, M. Schreiner: Constructive Approximation on the Sphere — With Applications to Geomathematics, Oxford University Press, Oxford, (1998).

[9] A. Amirbekyan: The Application of Reproducing Kernel Based Spline Approximation to Seismic Surface and Body Wave Tomography: Theoretical Aspects and Numerical Results, PhD thesis, published at http://kluedo.ub.uni-kl.de/volltexte/2007/2103/, (2007).

[10] A. Amirbekyan and V. Michel: Splines on the Three-dimensional Ball and Their Application to Seismic Body Wave Tomography, Inverse Problems, **24**, 015022(25pp), (2008).

[11] M.J. Fengler, D. Michel, V. Michel: Harmonic Spline-wavelets on the 3-dimensional Ball and Their Application to the Reconstruction of the Earth's Density Distribution From Gravitational Data at Arbitrarily Shaped Satellite Orbits, Zeitschrift für Angewandte Mathematik und Mechanik (ZAMM), **86**, 856-873, also published online at DOI:10.1002/zamm.200510277, (2006).

[12] V. Michel, K. Wolf: Numerical Aspects of a Spline-based Multiresolution Recovery of the Harmonic Mass Density out of Gravity Functionals, Geophysical Journal International, **173**, 1-16, (2008).

[13] P. Berkel: Multiscale Methods for the Combined Inversion of Normal Mode and Gravity Variations, PhD thesis, Shaker Verlag, Aachen, 2009.

[14] P. Berkel, D. Fischer, V. Michel: Spline Multiresolution and Numerical Results for Joint Gravitation and Normal Mode Inversion With an Outlook on Sparse Regularisation, International Journal on Geomathematics, **1**, 167-204, (2011).

[15] P. Berkel, V. Michel: On Mathematical Aspects of a Combined Inversion of Gravity and Normal Mode Variations by a Spline Method, Mathematical Geosciences, **42**, 795-816 (2010).

[16] P. Deuflhard: On Algorithms for the Summation of Certain Special Functions, Computing, **17**, 37-48, (1975).

[17] A.F. Nikiforov, V.B. Uvarov: Special Functions of Mathematical Physics — A Unified Introduction with Applications, translated from the Russian by R.P. Boas, Birkhäuser, Basel, 1988.

[18] G. Dassios and A.S. Fokas: Electro-Magneto-Encephalography for the three-Shell Model: Dipoles and Beyond for Spherical Geometry, Inverse Problems, **25**, (2009).

[19] A.S. Fokas and Y. Kurylev: Electro-magneto-encephalography for the Three-shell Model: Minimal L^2-norm in Spherical and Ellipsoidal Geometries (preprint).

[20] C. Michel, M. Murray, G. Lantz, S. Gonzalez, L. Spinelli, R. Grave de Peralta: EEG Source Imaging, Clinical Neurophysiology, **115**, 2195-2222, (2004).

[21] M.S. Hämäläinen and R.J. Ilmoniemi: Interpreting Magnetic Fields of the Brain: Minimum Norm Estimates, Medical & Biological Engineering & Computing, **32**, 35-42, (1994).

[22] O. Hauk: Keep it Simple: a Case for Using Classical Minimum Norm Estimation in the Analysis of EEG and MEG Data, Neuroimage, **21**, 1612-1621, (2004).

[23] I.F. Gorodnitsky, J.S. George, B.D. Rao, Neuromagnetic Source Imaging with FOCUSS: a Recursive Weighted Minimum Norm Algorithm, Electroencephalography and Clinical Neurophysiology, **15**, 231-251, (1995).

[24] R. Grave de Peralta Menendez, S.L. Andino Gonzalez, A Critical Analysis of Linear Inverse Solutions, IEEE Trans. Biomed. Eng., **45**, 440-448, (1998).

[25] R.D. Pascual-Marqui, C.M. Michel, D. Lehmann, Low Resolution Electromagnetic Tomography: a new Method for Localizing Electrical Activity in the Brain, International Journal of Psychophysiology, **18**, 49-65, (1994).

[26] R. Grave de Peralta Menendez, S.L. Gonzalez Andino, S. Morand, C.M. Michel, T. Landis, Imaging the Electrical Activity of the Brain: ELECTRA, Hum. Brain Mapp., **9**, 1-12, (2000).

[27] M.X. Huang, J.C. Mosher, R.M. Leahy, A Sensor-weighted Overlapping Sphere Head Model and Exhaustive Head Model Comparison for MEG, Phys. Med. Biol., **44**, 423-440, (1999).

[28] L. Spinelli, S.G. Andino, G. Lantz, M. Seeck, C. M. Michel, Electromagnetic Inverse Solutions in Anatomically Constrained Spherical Head Models, Brain Topogr., **13**, 115-125, (2000).

Siegen Preprints on Geomathematics

The preprint series “Siegen Preprints on Geomathematics” was established in 2010. See www.geomathematics-siegen.de for details and a contact address. At present, the following preprints are available:

1. P. Berkel, D. Fischer, V. Michel: *Spline multiresolution and numerical results for joint gravitation and normal mode inversion with an outlook on sparse regularisation*, 2010.
2. M. Akram, V. Michel: *Regularisation of the Helmholtz decomposition and its application to geomagnetic field modelling*, 2010.
3. V. Michel: *Optimally Localized Approximate Identities on the 2-Sphere*, 2010.
4. N. Akhtar, V. Michel: *Reproducing Kernel Based Splines for the Regularization of the Inverse Spheroidal Gravimetric Problem*, 2011.
5. D. Fischer, V. Michel: *Sparse Regularization of Inverse Gravimetry - Case Study: Spatial and Temporal Mass Variations in South America*, 2011.
6. A.S. Fokas, O. Hauk, V. Michel: *Electro-Magneto-Encephalography for the three-Shell Model: Numerical Implementation for Distributed Current in Spherical Geometry,* 2011.

Geomathematics Group Siegen
Prof. Dr. Volker Michel

Contact at:
Geomathematics Group
Department of Mathematics
University of Siegen
Walter-Flex-Str. 3
57068 Siegen
www.geomathematics-siegen.de

UNIVERSITÄT
SIEGEN

Angewandte Analysis, Numerik
Didaktik der Mathematik
Reine Mathematik, Informatik
Statistik, Risikoanalyse, Computing

Geomathematics Group